

Reversed two-cell convection in the Northern and Southern hemispheres during northward interplanetary magnetic field

G. Lu,¹ W. H. Li,² J. Raeder,² Y. Deng,³ F. Rich,^{4,5} D. Ober,⁵ Y. L. Zhang,⁶ L. Paxton,⁶ J. M. Ruohoniemi,⁷ M. Hairston,⁸ and P. Newell⁶

Received 1 August 2011; revised 27 October 2011; accepted 31 October 2011; published 31 December 2011.

[1] This article presents a case study of large-scale ionospheric convection in the Northern and Southern Hemispheres under strongly northward interplanetary magnetic field (IMF) conditions on 9 November 2004. Using a comprehensive data set from both ground- and space-based instruments, the study shows the formation of reversed two-cell convection in both the Northern and Southern Hemispheres that lasted for nearly 2 hours. Examination of the concurrent satellite energy-time spectrograms of precipitating particles reveals that reverse convection occurs in the region filled mostly with the boundary plasma sheet (BPS) type precipitating electrons except that the electron number flux is much smaller than that in the normal BPS. We have named this region the northward B_z boundary layer (NBZBL), which we interpret as a consequence of double-lobe reconnection. This interpretation is corroborated by the global MHD simulations, which show that the NBZBL consists of mostly closed field lines, resulting from double-lobe reconnection in both the hemispheres, together with intermittent presence of overdraped open field lines, resulting from single-lobe reconnection in one of the hemispheres. In addition to reversed two-cell convection, the distribution of field-aligned currents (FACs) shows clearly the presence of a pair of the northward B_z (NBZ) currents near the central polar region in both the hemispheres. Intense downward Poynting flux with a peak value around 100 mW/m^2 is also seen in the high-latitude polar region, which tends to surround the upward leg of the NBZ currents. Finally, the potential drop between the two reverse-convection cells exceeds 100 kV, which is far larger than the values reported in any previous studies of reverse convection under northward IMF conditions. The unusually large reverse potential drop in this case is attributed in part to the strong NBZ component of 35–40 nT and in part to the unusually large solar wind dynamic pressure that is about five times its nominal value.

Citation: Lu, G., et al. (2011), Reversed two-cell convection in the Northern and Southern hemispheres during northward interplanetary magnetic field, *J. Geophys. Res.*, 116, A12237, doi:10.1029/2011JA017043.

1. Introduction

[2] The morphology of high-latitude ionospheric convection depends strongly on the orientation of the interplanetary magnetic field (IMF). When the IMF B_z component is southward, the large-scale plasma flows form a two-cell circulation pattern, with the dawn cell in counter clockwise circulation and the dusk cell in clockwise circulation. Plasma flows are predominantly antisunward across the polar cap for southward IMF. When B_z is northward, the convection configuration becomes rather complex, consisting of either distorted two cells or multiple cells. In case of a multicell pattern, the two cells near the central polar cap are in reverse circulation as opposed to that under southward IMF conditions, namely, clockwise circulation on the dawnside and counter clockwise circulation on the duskside. Correspondingly, under northward IMF, plasma flows across the central polar cap are sunward instead of antisunward. This type of convection

¹High Altitude Observatory, National Center for Atmospheric Research, Boulder, Colorado, USA.

²Department of Physics and Space Science Center, University of New Hampshire, Durham, New Hampshire, USA.

³Department of Physics, University of Texas at Arlington, Arlington, Texas, USA.

⁴Massachusetts Institute of Technology Lincoln Laboratory, Lexington, Massachusetts, USA.

⁵Air Force Research Laboratory, Kirtland Air Force Base, New Mexico, USA.

⁶Johns Hopkins University Applied Physics Laboratory, Laurel, Maryland, USA.

⁷Department of Engineering, Virginia Polytechnic Institute and State University, Blacksburg, Virginia, USA.

⁸Center for Space Sciences, University of Texas at Dallas, Richardson, Texas, USA.

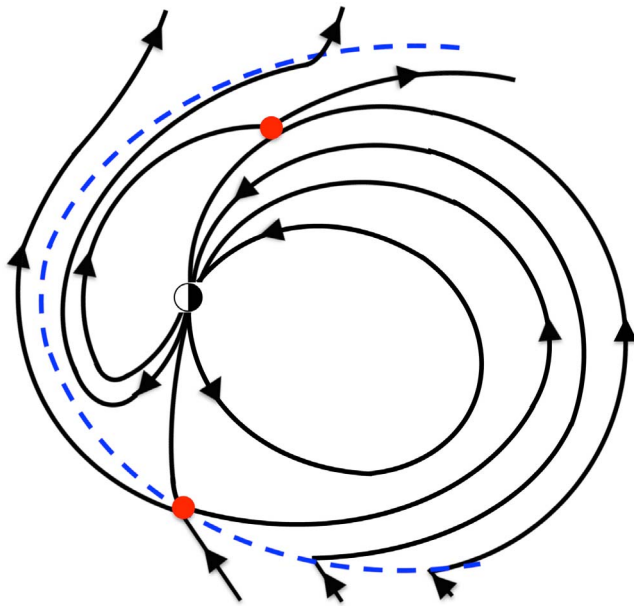


Figure 1. The noon-midnight meridional cross section of the magnetosphere corresponding to northward IMF condition. The blue dashed line represents the magnetopause, and the red dots denote the reconnection sites. Figure 1 is adapted from Figure 4 of Crooker [1992] but modified for the northern winter conditions.

configuration is dubbed “reverse convection” [e.g., Crooker, 1992].

[3] The formation of reverse convection has been postulated in terms of the overdraped lobe model [Crooker, 1992], which was developed from the conceptual magnetic reconnection models proposed first by Dungey [1963] and later by Cowley [1981, 1983]. Figure 1 depicts the magnetospheric topology in the noon-midnight meridional plane. It is adopted from Figure 4 of Crooker [1992] but modified for northern winter conditions. On the basis of the overdraped lobe model, magnetic reconnection preferably takes place in the Southern (Summer) Hemisphere where an interplanetary field line merges with a closed plasma sheet field line just poleward of the southern cusp. The newly opened field line then drapes over the dayside magnetopause, and the magnetic tension force exerted on the field line brings the plasma sunward together with the field line. A second reconnection can take place in the Northern (Winter) Hemisphere where the draped field line merges with an open-lobe field line, forming a closed field line on the dayside and a detached field line on the nightside that eventually is carried away by the solar wind. The northern reconnection is most permissible when the IMF B_x component is negative, opposite to the x component of geomagnetic field poleward/tailward of the northern cusp. It is possible that the draping of field lines over the dayside magnetopause may effectively reduce the B_x and seasonal dependence of lobe reconnection. Though Figure 1 depicts specifically the IMF reconnecting with closed plasma sheet field lines, the same process is readily applicable with open-lobe field lines, such as described by Milan *et al.* [2000] and Imber *et al.* [2006]. This concurrent high-latitude reconnection process in both the hemispheres, which is also referred as double-lobe reconnection, thus

produces sunward plasma flows in both the northern and southern polar regions. Double-lobe reconnection is expected to occur when the IMF clock angle is small [Crooker, 1992; Provan *et al.*, 2005; Imber *et al.*, 2006].

[4] Lobe reconnection is primarily a summer phenomenon [Crooker and Rich, 1993]. Indeed, the reversed two-cell convection configuration is often found in the Summer Hemisphere, whereas weak, distorted, convection is typically seen in the Winter Hemisphere under northward IMF [e.g., Bythrow *et al.*, 1985; Knipp *et al.*, 1993; Lu *et al.*, 1994]. Sunward plasma flows have been observed in the Northern and Southern Hemispheres under northward IMF conditions [Reiff, 1982; Cumnock *et al.*, 1995; Imber *et al.*, 2006; Hu *et al.*, 2006]. However, the reversed two-cell convection patterns that form simultaneously in both the hemispheres have rarely been reported partly because of the fortuitous seasonal and IMF conditions that are required for such events and partly because of the inadequate global coverage of observations. Using the Super Dual Auroral Radar Network (SuperDARN), Provan *et al.* [2005] presented a case study of a four-cell convection pattern, with two reversed cells at high latitudes and two “normal” cells at lower latitudes, in the Northern Hemisphere when IMF B_z was strongly northward (i.e., $B_z/|B_y| > 1$). Unfortunately, owing to the lack of adequate radar backscatter in the Southern Hemisphere, they were unable to construct the global convection pattern even though the Southern Hemisphere was in the more favorable summer condition. It should be noted that the presence of sunward convection does not always invoke the formation of the reversed two-cell convection pattern [Cumnock *et al.*, 1995]. Global observations are required to unambiguously characterize the large-scale ionospheric convection configuration under various IMF orientations.

[5] The overdraped lobe model predicts that reverse convection can occur simultaneously in both the hemispheres when one hemisphere has the seasonal preference, while the other hemisphere has the IMF B_x preference. The event that we present here was one such propitious occurrence. The event took place on 9 November 2004, when a fast-moving interplanetary coronal mass ejection (ICME) impinged on the Earth’s magnetosphere [Richardson and Cane, 2010]. Within the leading edge of the ICME, the IMF B_z component was strongly northward for several hours and B_x was negative. Thus, while the seasonal condition (e.g., southern summer) helps reverse convection to form in the Southern Hemisphere, the negative B_x condition facilitates reverse convection in the Northern Hemisphere. This study shows clearly the formation of the reversed two-cell convection patterns in both the Northern and Southern Hemispheres for nearly 2 hours following the northward turning of the IMF in association with the leading edge of the ICME. As demonstrated by Deng *et al.* [2009], the reverse plasma convection during this event was strong enough and lasted long enough to alter thermospheric neutral winds owing to ion drag forces on neutral gases.

2. Observations and Modeling Results

2.1. Solar Wind and Geophysical Conditions

[6] Figure 2 shows the solar wind and geophysical conditions from 16:00 UT on 9 November 2004 to 02:00 UT on

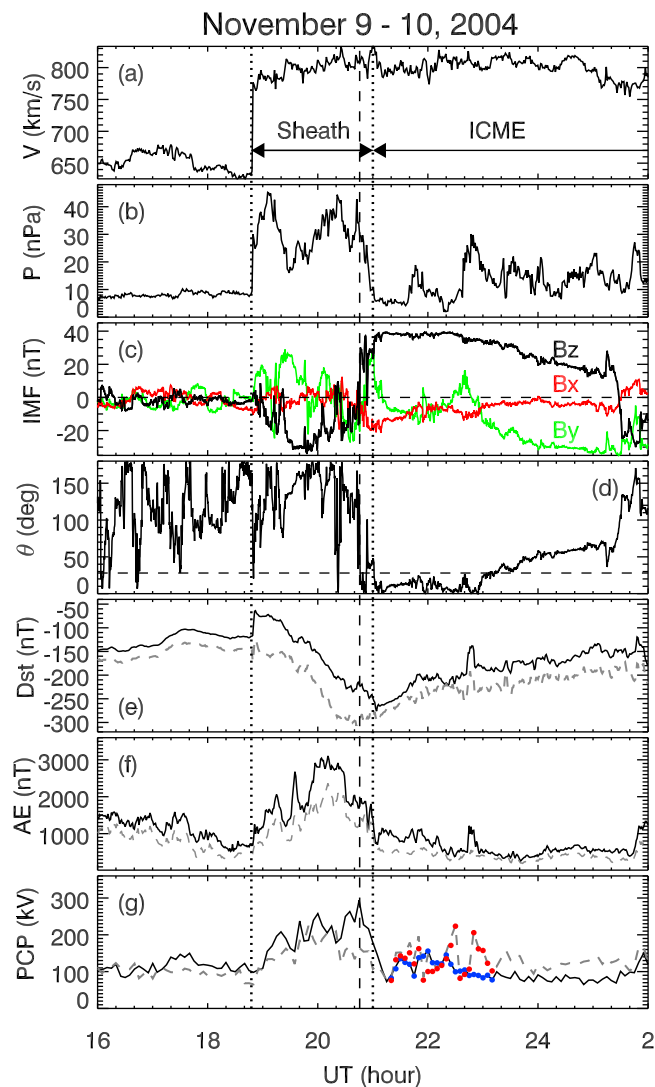


Figure 2. Solar wind and geophysical parameters for the period from 16:00 UT on 9 November to 02:00 UT on 10 November 2004: (a) the solar wind bulk speed; (b) the solar wind dynamic pressure; (c) the IMF B_x , B_y , and B_z components in GSM coordinates; (d) the IMF clock angle; (e) the Dst index in solid line and the solar wind dynamic pressure corrected Dst (Dst^*) in dashed line; (f) the AE index in solid line and the reversed AL (i.e., $-AL$) index in dashed line; and (g) the cross-polar-cap potential drops in the Northern Hemisphere (solid) and Southern (dashed) Hemisphere. The blue and red dots in Figure 2g represent the potential drops between the two reversed convection cells. A time lag of 28 min has been applied to the solar wind and IMF data from the ACE spacecraft. The horizontal dashed line in Figure 2d corresponds to a clock angle of 28° .

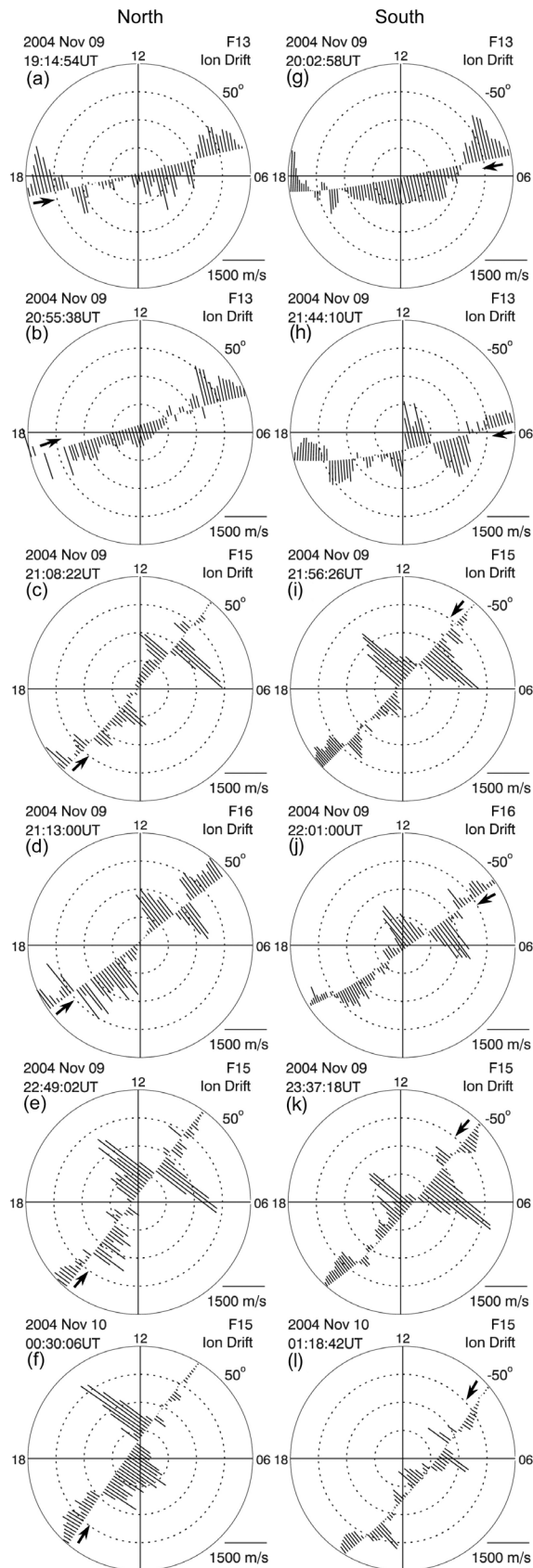
10 November 2004. Figures 2a and 2b show the solar wind bulk speed and dynamic pressure, respectively. An interplanetary shock (IPS) arrived at 18:49 UT when the solar wind speed jumped from ~ 600 to more than 750 km/s. Figure 2c shows the IMF in GSM coordinates. The B_z component turned sharply northward at 20:46 UT on 9 November and remained northward until about 01:30 UT

on 10 November. During this time interval, the IMF B_x component was negative, a favorable condition for lobe reconnection in the Northern Hemisphere [Crooker, 1992]. The interval between 18:49 and 21:00 UT was the sheath region, where the background solar wind is compressed by the fast-moving ICME from behind. Inside the sheath region, the solar wind dynamic pressure was highly elevated, and B_z was mainly southward with a minimum value of about -30 nT, while both B_x and B_y were fluctuating between positive and negative values. Figure 2d shows the IMF clock angle θ , which is defined as $\theta = \tan^{-1}(|B_y|/B_z)$. The horizontal dashed line in Figure 2d corresponds to a clock angle of 28° . Previous studies have shown that double-lobe reconnection takes place when the IMF clock angle is less than 10° . However, as we will show in section 2.3, reversed two-cell convection has been observed in both the Northern and Southern Hemispheres when the IMF clock angle is as large as 28° . A plausible cause is discussed in section 3.

[7] The Dst index is a measure of geomagnetic activity at low latitudes and is commonly used as a gauge of the ring current intensification during geomagnetic storms. Other currents also contribute to the Dst index, most importantly the magnetopause current that produces northward or positive magnetic perturbations on the surface of the Earth at low latitudes. Figure 2e shows the Dst index for the interval. Note that the Dst index used in this study is obtained from a worldwide network of 52 stations located below $|40^\circ|$ magnetic latitude (MLAT) and has a time cadence of 1 min. The arrival of the IPS prompted a sudden rise or positive excursion in the Dst index at 18:49 UT associated with the enhanced solar wind dynamic pressure and thus enhanced magnetopause current. To remove the contribution of the magnetopause current, we apply the formula of Burton *et al.* [1975], for example, $Dst^* = Dst - 16\sqrt{P} + 20$, where P is the solar wind dynamic pressure in nanopascal. The solar wind dynamic pressure corrected Dst (or Dst^*) is shown as the dashed line in Figure 2e.

[8] As the solar wind and IMF measurements were made by the ACE spacecraft located at about $(242, 22, -15) R_E$ in GSE coordinates, a time shift of 28 min has to be applied to the ACE data plotted in Figure 2 to account for the solar wind propagation from its upstream location to the magnetosphere. This time shift is estimated by applying the Burton formula to eliminate the positive excursion in Dst associated with the enhanced magnetopause current induced by the solar wind pressure impulse. As the ACE plasma data are in a 64 s time resolution, and the multi-station derived Dst is in a 1 min resolution, the estimated solar wind propagation time based on the Dst^* profile thus yields an accuracy of approximately 1 min. For comparison, the convectional x -distance propagation method calculates the lag time from $t = (L_1 - L_0)/V_x$. Taking the ACE distance L_0 at $242 R_E$, the dayside magnetopause location L_1 at $10 R_E$, and an average speed V_x of 780 km/s for the fast solar wind stream, one obtains a lag time of approximately 32 min. Additional time of 2–3 min is often added to account for the slowdown of the solar wind in the magnetosheath. This leads to a total lag time of 34–35 min.

[9] The auroral electrojet (AE) index (solid line) and the reversed AL (or $-AL$) value (dashed line) are shown in Figure 2f. These indices are also at a 1 min cadence, derived



from the north-south component of ground magnetic perturbations at 80 stations located between 155° and 176° MLATs in the Northern and Southern Hemispheres. During the interval of southward IMF, the maximum value of AE reached 3000 nT during the sheath interval. After B_z turned northward, AE dropped mostly below 1000 nT. Although the AE value was still higher than the normal quiet geomagnetic condition, it remained relatively steady throughout the northward B_z (NBZ) interval except a few excursions in association with the solar wind dynamic pressure enhancements. The AL index remained at a nearly constant value of 400 nT during northward IMF.

[10] Figure 2g shows the cross-polar-cap potential drops in the Northern Hemisphere (solid line) and Southern Hemisphere (dashed line), respectively. The cross-polar-cap potential drop is defined as the difference between the maximum and minimum potentials over the entire polar region as derived using the assimilative mapping of ionospheric electrodynamics (AMIE) procedure [Richmond and Kamide, 1988] (see section 2.3 for more details). The cross-polar-cap potential drop was about 200–300 kV in both the hemispheres during the period of the sheath encounter when the IMF B_z component was strongly southward and reduced to approximately 100 kV after B_z turned northward. Overlaid on the cross-polar-cap potential drops are the potential drop between the two reverse-convection cells, with the blue dots representing the reverse potential drop in the Northern Hemisphere and the red dots representing the reserve potential drop in the Southern Hemisphere. During the interval of strongly NBZ between 21:20 and 23:10 UT, reverse convection dominated the overall ionospheric convection configuration, so that the reverse potential drop becomes nearly the same as the total cross-polar-cap potential drop.

2.2. DMSP Observations

[11] The DMSP spacecraft is in the Sun-synchronous near-polar orbit at an altitude of approximately 840 km. The spacecraft has an orbital period of 101 min, and it takes about 15–20 min, depending on the satellite trajectory to cross the polar region above 150° MLAT. The ion drift data used in this study were obtained by the ion drift meter, which is part of the Special Sensor for Ions and Electrons [Heelis and Hairston, 1990]. More detailed information on the analysis techniques for the DMSP ion drift data can be found in Hairston and Heelis [1993]. Figure 3 shows the cross-track ion drifts measured by the different DMSP spacecraft, for example, F13, F15, and F16. In each panel, the arrow indicates the travel direction of the spacecraft, and the marked UT corresponds to the time when the spacecraft was closest to the magnetic pole in the respective hemisphere. The left column is for the Northern Hemisphere passes, and the right column for the Southern Hemisphere

Figure 3. Cross-track ion drifts measured by the DMSP spacecraft: (a–f) the northern hemispheric passes and (g–l) the southern hemispheric passes. Note that the northern and southern passes were not simultaneous, and the marked UT in each panel corresponds to the time when the spacecraft was closest to the magnetic pole in the respective hemisphere. The arrows indicate the travel direction of the spacecraft.

passes. Note that the cross-track ion drifts are plotted in MLAT versus magnetic local time, and the Northern and Southern Hemisphere passes are at different UT times as indicated in each panel. Prior to the IMF B_z northward turning, as shown in Figures 3a and 3g, DMSP F13 observed antisunward convection over the polar cap and sunward convection at lower latitudes in both the hemispheres. Shortly after the B_z northward turning at 20:46 UT, F13 passed the Northern Hemisphere again (Figure 3b), measuring weak sunward flows on the dawnside of the polar region from 76° to 80° MLAT where flows were antisunward during the previous polar passing (Figure 3a). Even stronger sunward flows were observed in the southern polar region, as shown in Figure 3h, where the sunward flow speed exceeded 1000 m/s. Sunward convection was observed during all subsequent DMSP polar passes in both the hemispheres until about 01:18 UT on the next day of 10 November. However, as discussed in section 2.3, sunward convection does not necessarily constitute the formation of the reversed two-cell convection configuration.

[12] Along with the changes in plasma convection following the B_z northward turning, the corresponding plasma characteristics also underwent significant alterations. The Special Sensor Precipitating Electron and Ion Spectrometer (SSJ/4) particle detector on board the DMSP spacecraft measures precipitating electron and ions from 32 eV to 30 keV in 19 logarithmically spaced energy channels [Hardy *et al.*, 1984]. On the basis of the electron and ion energy spectra, the different plasma regimes can be identified. In this article, we follow the criteria similar to those proposed by Newell and colleagues [e.g., Newell and Meng, 1992; Newell *et al.*, 1991]. Polar rain consists of electrons up to a few hundred electron volts. The cusp is identified by its enhanced ion energy flux, which typically exhibits a distinctive energy dispersion feature. The boundary plasma sheet (BPS) maps to the high-latitude plasma sheet boundary layer and is associated with discrete aurora produced by accelerated precipitating electrons with energies greater than 1 keV. The central plasma sheet (CPS), on the other hand, is commonly associated with diffuse aurora. The main difference between the CPS and BPS is that the precipitating electrons tend to be more structured in the BPS than in the CPS.

[13] Figure 4 displays the energy-time spectrograms from the two consecutive southern passes by F15 before and after the B_z northward turning. Also plotted are the cross-track ion drifts in Figure 4a, and magnetic field perturbations along (blue curve) and perpendicular (black curve) to the satellite trajectory in Figure 4b. Sunward ion drifts are represented by positive values and antisunward ion drifts by negative values. For magnetic field perturbations, positive values represent the components along and to the right of the satellite trajectory, respectively. The red curve in Figure 4b is field-aligned current (FAC) density derived from the gradient of the perpendicular magnetic field perturbation, with positive values for currents flowing into the ionosphere (downward) and negative values for currents flowing out of the ionosphere (upward).

[14] Prior to the B_z northward turning (Figure 4a), F15 encountered the CPS followed by a narrow cusp region in the prenoon sector as manifested by intense precipitating ions. The spacecraft then crossed a broad zone of polar rain

filled with low-energy (a few hundred electron volts) precipitating electrons. Finally, the spacecraft entered the BPS on the nightside. The intense ion precipitation in the cusp was embedded in a region of downward FAC as indicated by the red curve in the second panel. Over the polar cap, ion drift was antisunward, and there were almost no FACs flowing into or out of the polar cap. It should be noted that the sharp drop in ion energy flux below 1 keV in the DMSP F15 ion energy-time spectrogram is caused by a loss of sensitivity in the 30 eV–1 keV channels due to degradation.

[15] After B_z turned northward (Figure 4b), ion drift became strongly sunward near the central polar region. The F15 spacecraft observed an extended region of the BPS plasma characteristics on the dayside. Poleward of the BPS was the cusp with intense precipitating ions. Note that the cusp had moved from -62° MLAT during the previous polar crossing shown in Figure 4a when the IMF was southward, to about -89° MLAT at the poleward edge of the sunward convection zone. The precipitating ions exhibited a V-shaped structure as the spacecraft was traversing the cusp on the dawnside and moving toward the south magnetic pole. Previous studies [e.g., Reiff *et al.*, 1980; Burch *et al.*, 1980] have found the V-shaped cusp signature to be predominantly associated with northward IMF and attributed this peculiar feature to cross-field diffusion that causes particles with larger perpendicular energies to scatter further away from the injection field line [Reiff *et al.*, 1977]. It is also worthwhile noting that the electrons in the vicinity of the cusp are very similar to the BPS electrons whose energy is higher than the normal cusp electrons under southward IMF as shown in Figure 4a, which implies that these electrons are not directly injected from the solar wind. One may take this as an evidence that the cusp shown in Figure 4b was a result of reconnection between the IMF and the closed plasma sheet field lines, as postulated in section 1. The V-shaped cusp also corresponds to downward FAC. As shown later in Figure 7d, the cusp feature observed by F15 coincides with the bright auroral emission near the south magnetic pole by the scanning auroral imager on board the DMSP F16 spacecraft.

[16] The strong sunward convection zone on the dayside resided partly within the BPS and partly in the cusp. On the nightside, the spacecraft encountered the BPS and CPS below about -67° MLAT. Between the dayside cusp and the nightside BPS was a region filled with the BPS-type precipitating electrons of a few keV except that the electron number flux was much smaller compared to the normal BPS. Also different from the normal BPS was the lack of significant precipitating ions. An auroral arc was clearly visible within this region. To distinguish it from the normal BPS, we shall call this region the northward B_z boundary layer (NBZBL). Similarly complex plasma features have been reported by Eriksson *et al.* [2006] during a transpolar auroral arc event associated with strongly northward IMF, which they interpreted as a region of the BPS/low-latitude boundary layer mixed with polar rain. The automated DMSP plasma boundary identification tool (<http://sd-www.jhuapl.edu/Aurora/spectrogram/index.html>) would mark a large portion of the region as the BPS and would consider it primarily a closed field line region [e.g., Newell *et al.*, 1997]. Others, on the other hand, have classified this region as the open polar cap [e.g., Provan *et al.*,

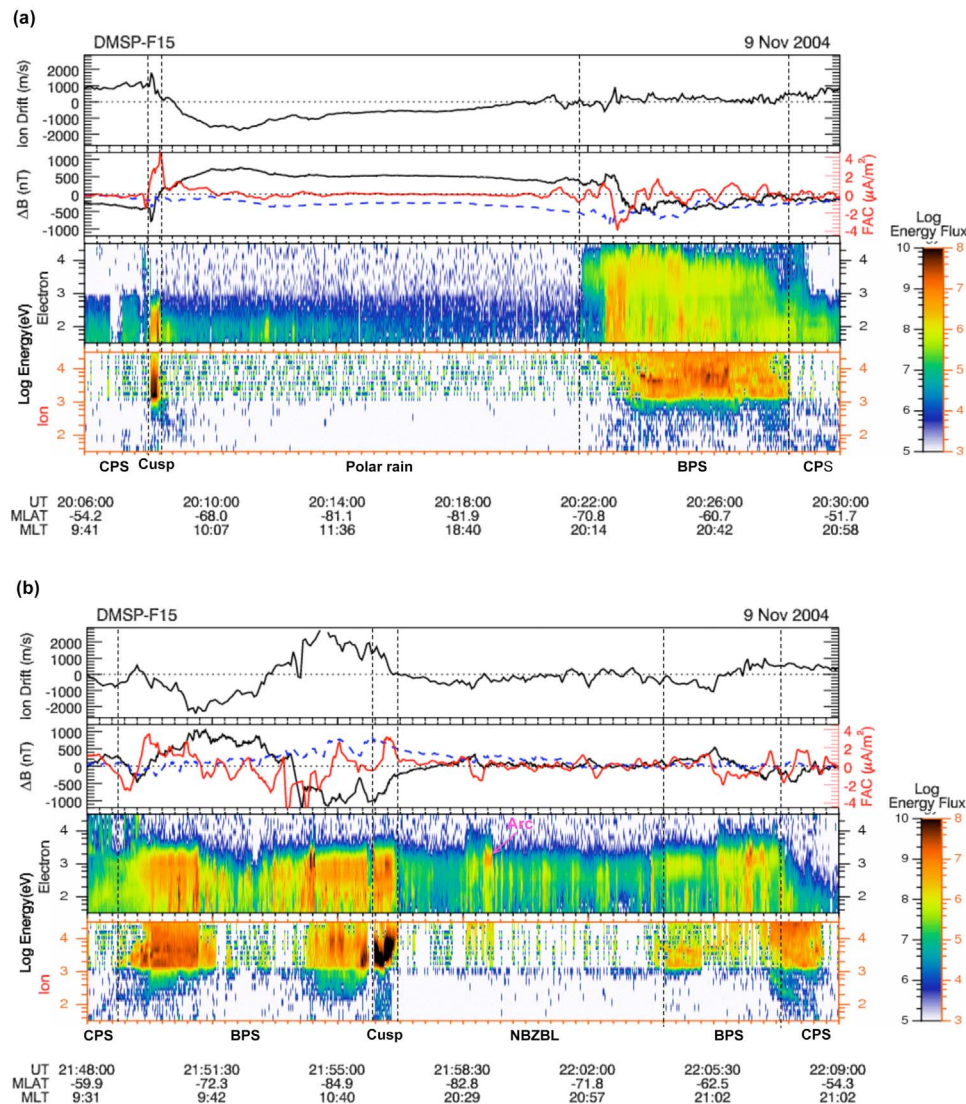


Figure 4. DMSP F15 observations during two consecutive southern passes: (a) from 20:06 to 20:30 UT and (b) from 21:48 to 22:09 UT. The first panel shows the cross-track ion drifts, with positive value for sunward flow and negative value for antisunward flow. The second panel shows the cross-track (black) and along-track (blue) magnetic field components, along with FAC (red) derived from the gradient of the cross-track component of magnetic field perturbations. The third and fourth panels are the energy-time spectrograms of electrons and ions, respectively. The vertical dashed lines demarcate the different plasma regimes.

2005]. Whether this region is open or closed is not crucial by itself, but we will discuss its implication on the solar wind-magnetosphere coupling process later in section 3.

2.3. Global Ionospheric Response

[17] To study the global ionospheric response to the strongly northward IMF conditions, we have used the AMIE procedure to derive the ionospheric convection patterns in both the Northern and Southern Hemispheres simultaneously. For this event, the data input to AMIE includes magnetic perturbations from 189 ground magnetometers worldwide, auroral precipitating electrons measured by three DMSP (e.g., F13, F15, and F16) and three NOAA (e.g., NOAA 15, 16, and 17) satellites, auroral images from the Global Ultraviolet Imager (GUVI) on the Thermosphere

Ionosphere Mesosphere Energetics and Dynamics (TIMED) spacecraft [Christensen *et al.*, 2003] and the Special Sensor Ultraviolet Spectrographic Imager (SSUSI) on board the DMSP F16 spacecraft [Paxton *et al.*, 2002], together with ion drift measurements from the DMSP spacecraft and the SuperDARN, which had eight radars operating in the Northern Hemisphere and five in the Southern Hemisphere at that time. The AMIE procedure is an optimally constrained, weighted least squares fit of coefficients to observations. It first modifies statistical conductance models [e.g., Fuller-Rowell and Evans, 1987] by incorporating the DMSP and NOAA particle data and the GUVI and SSUSI aurora images. More detailed information on auroral conductance modification is given by Richmond and Kamide [1988]. After the modified distributions of Pedersen and Hall

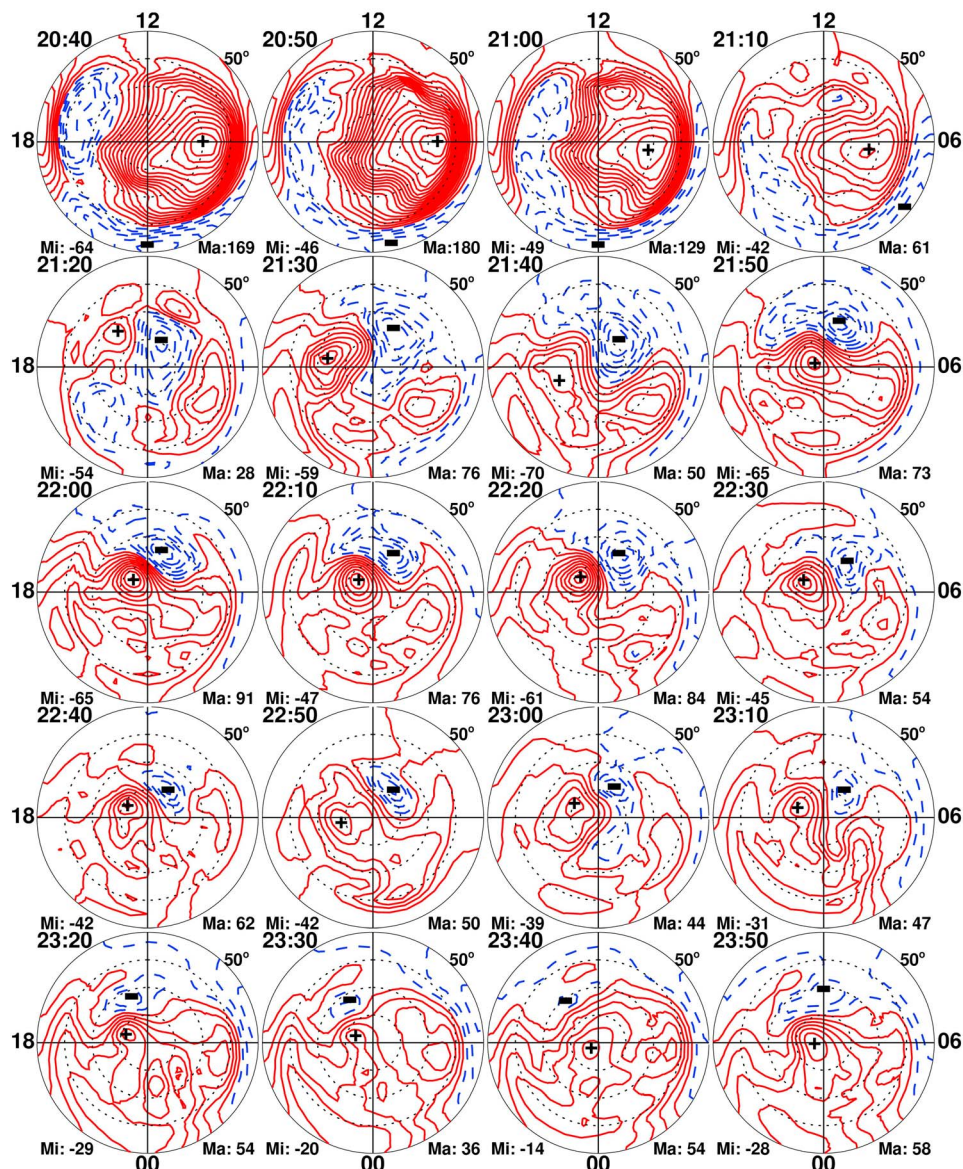


Figure 5. Consecutive ionospheric convection patterns from 20:40 to 23:50 UT in the Northern Hemisphere, with a contour interval of 10 kV. The positive and negative values below each pattern correspond to the electric potentials in the locations marked by the “+” and “-” signs, which are not necessarily the maximum and minimum potentials.

conductances are derived, then in a second step, the procedure obtains ionospheric convection, currents, and other related electrodynamic parameters by fitting simultaneously to measurements of ion drift and magnetic perturbations on ground and in space. A priori statistical electric potential model is often used to provide a first-order estimation in regions where no measurements otherwise exist. In this case, we use the statistical model based on the Millstone Hill radar measurements [e.g., *Foster et al.*, 1986], and the same background model is applied to the AMIE patterns for both the hemispheres. This model is essentially a normal two-cell convection pattern regardless of the IMF orientation, and its cross-polar-cap potential drop is parameterized based on the hemispheric power index [*Fuller-Rowell and Evans*, 1987]. More detailed information on the AMIE procedure,

including data ingestion and validation, can also be found in *Lu et al.* [1996, 2001].

[18] Figures 5 and 6 show a series of consecutive ionospheric convection patterns from 20:40 to 23:50 UT on 9 November in the Northern and Southern Hemispheres, respectively. After the B_z northward turning at 20:46 UT, the convection patterns started to change from the original two-cell configuration. By 21:20 UT, a pair of reverse-convection cells had developed in the polar regions of both the hemispheres. The reversed two-cell convection configuration lasted until 23:10 UT when the magnitudes of both B_x and B_z started to decrease and the magnitude of the IMF B_y component started to increase. From 23:20 UT and onward, the alignment of the two main convection cells had rotated roughly 90° counter clockwise in the Northern

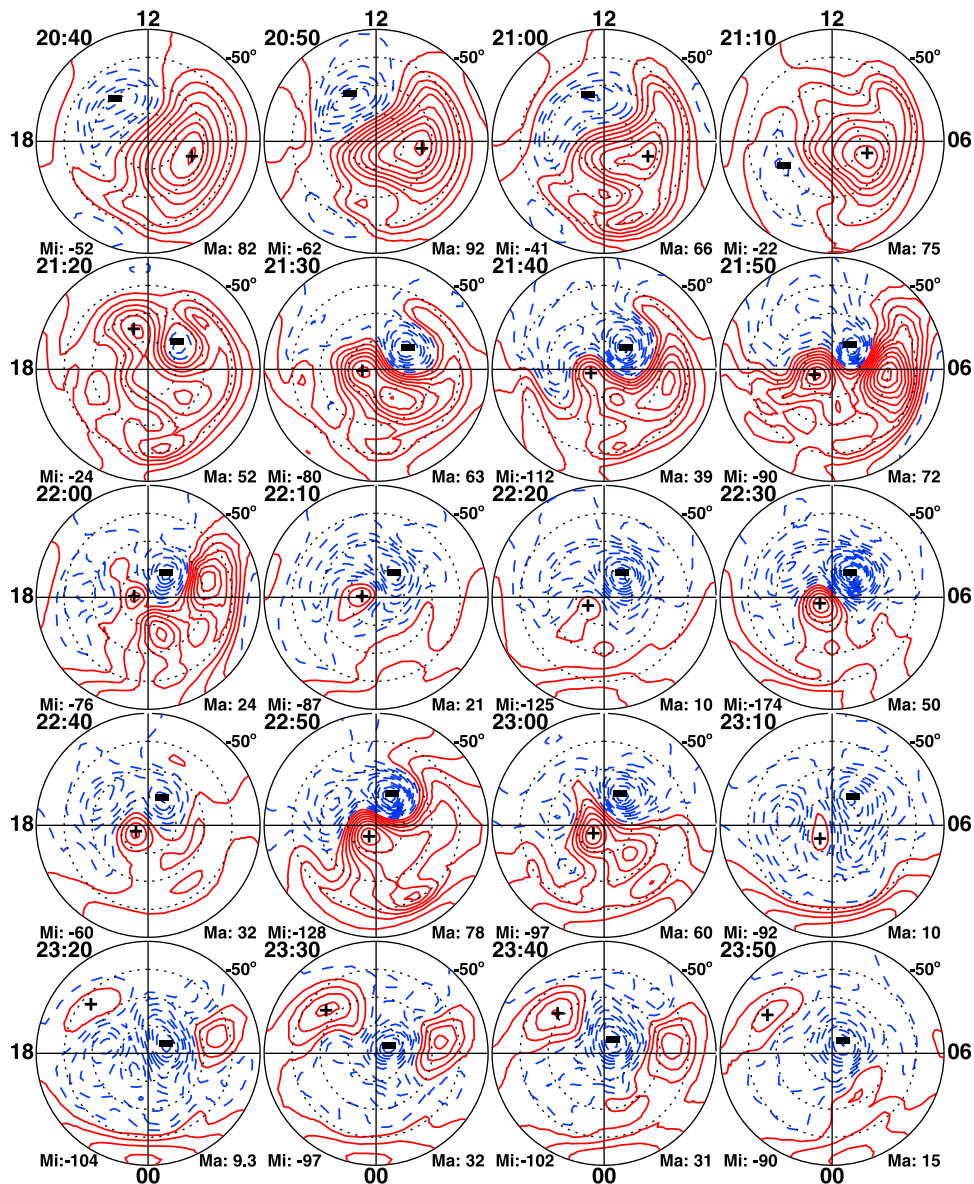


Figure 6. Same as Figure 5 but in the Southern Hemisphere.

Hemisphere and about 90° clockwise in the Southern Hemisphere, an indication of the IMF B_y effect. However, plasma flows near both magnetic poles remained mostly sunward as continually observed by the DMSP spacecraft (e.g., Figures 3k and 3f). Figures 5 and 6 show clearly the formation of large-scale reversed two-cell convection in both the Northern and Southern Hemispheres that lasted for nearly 2 hours.

[19] Figure 7 examines the distributions of various ionospheric fields at 22:05 UT in the Southern Hemisphere. The top row displays the AMIE patterns of plasma convection, FACs, and Poynting flux, along with auroral emissions at the Lyman-Birge-Hopfield short filter (LBHS) from the SSUSI instrument [Paxton *et al.*, 2002]. A pair of FACs are easily discernible near the central polar cap in Figure 7b, which are closely associated with the reverse-convection cells, with upward current (in blue) in the region of clockwise plasma convection (dashed contours) and downward

current (in red) in the region of counter clockwise convection (solid contours). Because they often form under NBZ conditions, this pair of FACs has been denoted as the NBZ currents [Iijima *et al.*, 1984]. At lower latitudes, FACs possess many small-scale structures, making the identification of region 1 and 2 currents rather difficult. Figure 7c shows the distribution of downward Poynting flux derived from AMIE. It is worth pointing out that the large downward Poynting flux is seen surrounding rather than at the center of the upward NBZ current.

[20] The F16 SSUSI instrument measures auroral emissions at five different wavelength bands. Figure 7d is a scanning image at the LBHS band of 140–150 nm, which is produced by excited N_2 through collisions with energetic electrons and ions. The image was taken over the period from 21:50 to 22:14 UT when F16 was traversing the Southern Hemisphere. Figure 7d shows auroral emissions at lower latitudes, along with two faint auroral arcs near the

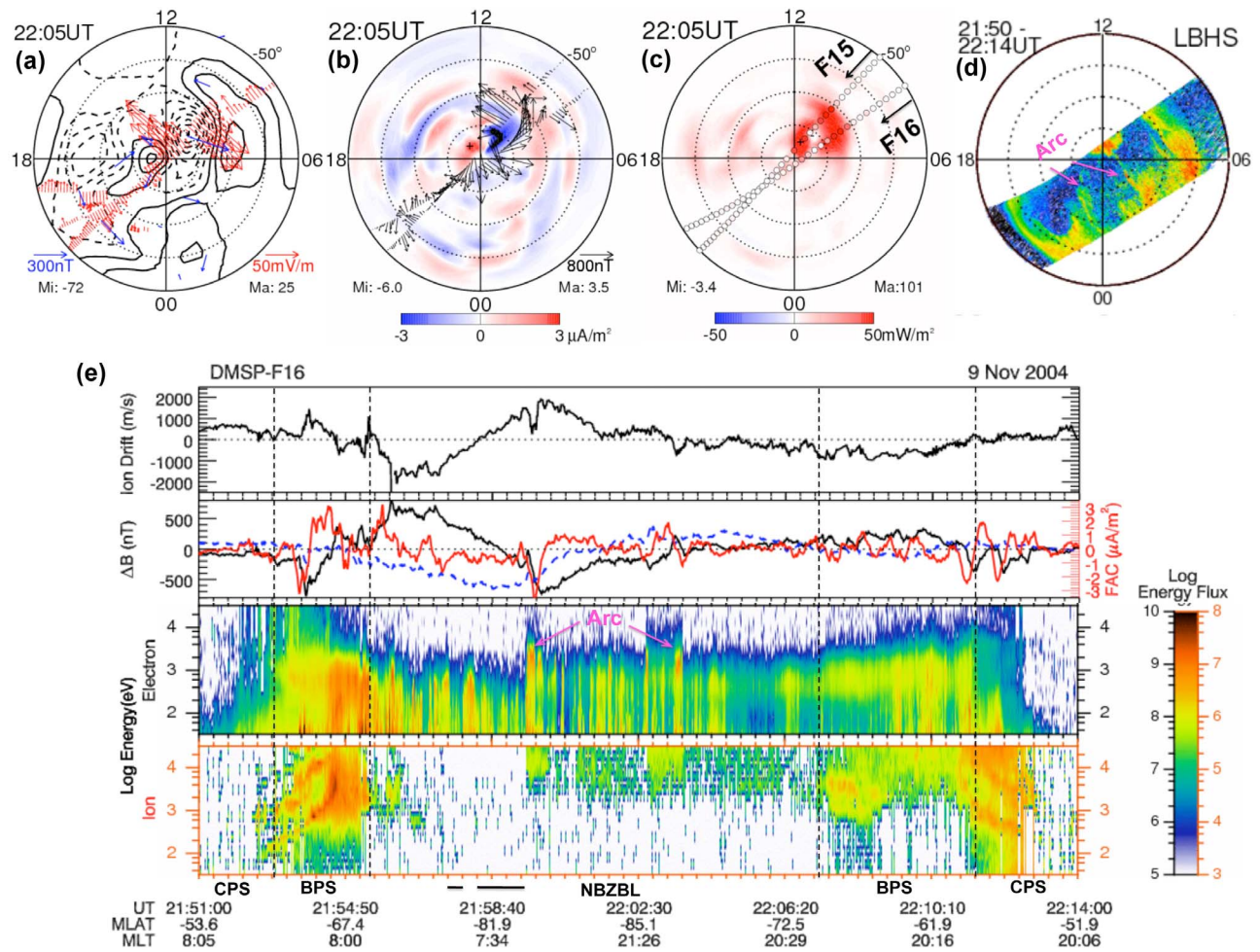


Figure 7. Distributions of (a) plasma convection, (b) FACs, (c) the Poynting flux, (d) auroral image by the F16 SSUSI instrument, and (e) measurements from DMSP F16 in the Southern Hemisphere around 22:05 UT. Note that downward FAC and Poynting flux are shown as positive values. The horizontal bars on the bottom indicate polar rain precipitation.

central polar region in the Southern Hemisphere. The most notable feature, however, is the relatively bright emission near the south magnetic pole. Because of its limited viewing angle, SSUSI was unable to reveal the spatial extent of this bright emission toward the dayside. Unfortunately, no global auroral images were available during this northward IMF interval to complement the SSUSI observations. This bright aurora appears to coincide with the enhanced downward Poynting flux at the central polar region. The energy flux associated with the bright emissions is estimated (based on the algorithm of *Zhang and Paxton* [2008]) to be about 23 mW/m^2 , whereas the Poynting flux in the same region peaks at 101 mW/m^2 . The majority of the Poynting flux from the magnetosphere is converted to Joule heating, and a small fraction goes to the acceleration of neutral winds [e.g., *Thayer et al.*, 1995; *Lu et al.*, 1995]. Note that the Poynting flux has a minimum value of -3.4 mW/m^2 , which corresponds to the upward Poynting flux adjacent to the peak of downward Poynting flux. Physically, upward Poynting flux can be generated by the neutral wind dynamo in regions where neutral winds are in the different direction than ion drifts [e.g., *Lu et al.*, 1995]. As the AMIE procedure neglects

neutral winds, the negative Poynting flux value is likely due to either a small baseline offset in the estimated magnetic field perturbations by AMIE or the “fringing field” effect associated with the 3-D ionospheric currents [*Richmond*, 2010].

[21] Also shown in Figure 7 are several measurements made by the DMSP F16 spacecraft, including the cross-track ion drift, the magnetic field perturbations as well as FACs derived from the gradient of the magnetic field component perpendicular to the satellite trajectory, and the energy-time spectrograms of precipitating electrons and ions. Similar to the F15 measurements shown in Figure 4b, the polar region was filled with discrete electron precipitation but very little ion precipitation (except in the vicinity of auroral arcs). In addition, intermittent polar rain precipitation can be seen in narrow zones (indicated by the horizontal bars on the bottom) around 21:57 and 21:59 UT, respectively. Again, we denote this region as the NBZBL. As illustrated in Figure 7b, the two DMSP spacecraft, F15 and F16, straddled the upward NBZ current rather than directly passing through it.

[22] Figure 8 shows the selected ionospheric patterns at 22:55 UT when the DMSP spacecraft passed over the

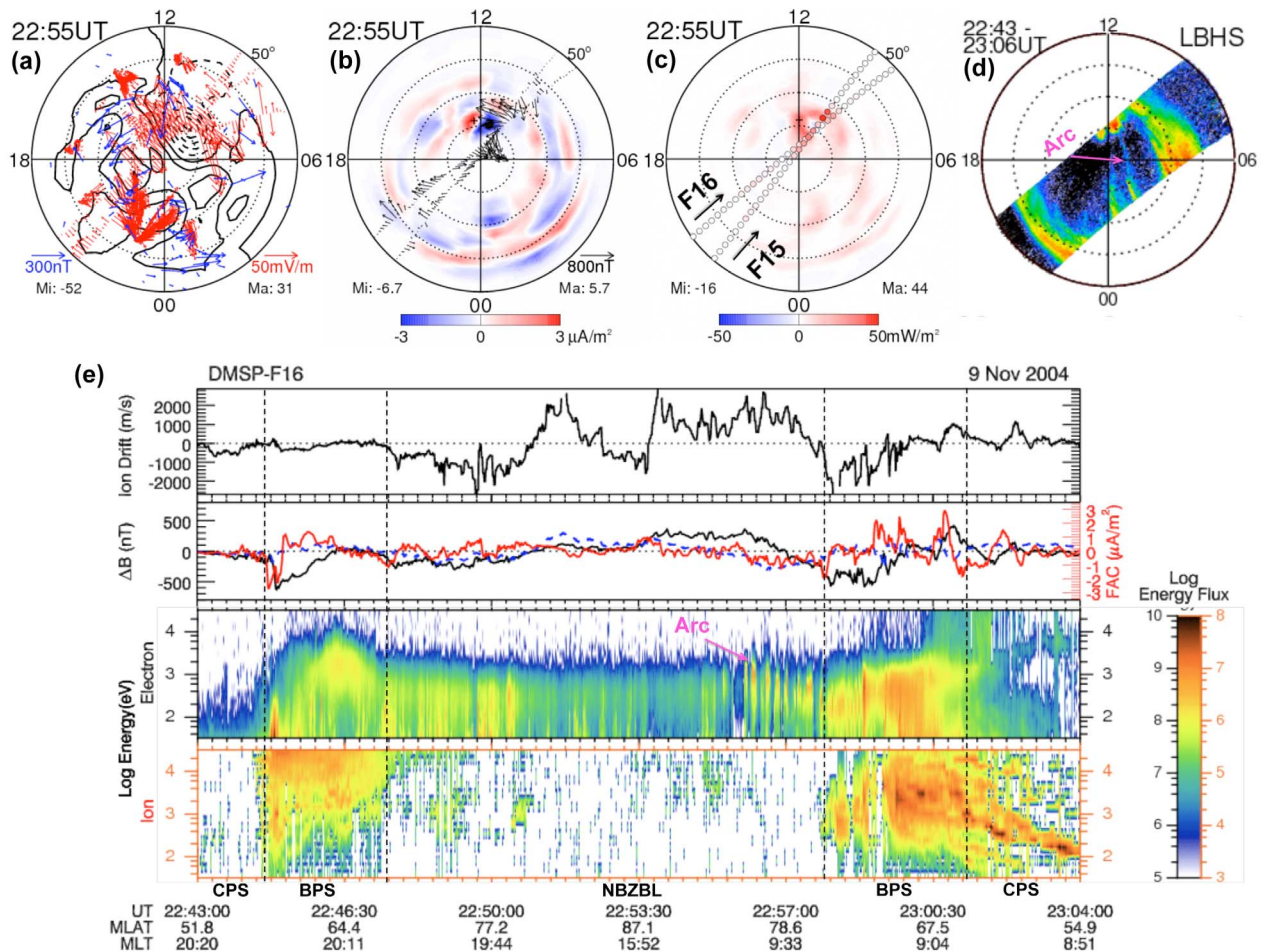


Figure 8. Same as Figure 7 but for the Northern Hemisphere at around 22:55 UT.

Northern Hemisphere. Similar to the southern hemispheric patterns shown in Figure 7, the reversed two-cell convection dominates the northern polar region. A pair of NBZ currents is also apparent but located further toward the dayside compared to that in the Southern Hemisphere. The two DMSP spacecraft passed over the northern polar region just tailward of the main NBZ currents, consistent with the fact that the FACs inferred from the DMSP magnetic field measurements were rather small. Two faint auroral arcs were captured by SSUSI. Both were located on the nightside of the dawn-dusk meridian, so that only one of the arcs was encountered by the in situ particle detector on the DMSP F16 spacecraft. The in situ particle detector, on the other hand, indicates at least three more arcs existing between these two main arcs, but they are too faint to show up in the SSUSI image. The time-energy spectrogram shown in Figure 8e is also very similar to Figure 7e, with the NBZBL occupying the polar region and the CPS and BPS at lower latitudes. However, no polar rain-type precipitation was discernable within the NBZBL during this pass.

[23] To assess the quality of the AMIE fitting, Figures 9 and 10 show the comparison of several key parameters inferred from the DMSP measurements with those derived from the AMIE procedure. In each figure, the along-track E-field is shown in the first panel, the cross-track magnetic

field perturbation is shown in the second panel, FACs are shown in the third panel, and the Poynting flux is shown in the fourth panel. A comparison with the F15 data is shown in the left column, and a comparison with the F16 data is shown in the right column. Note that the DMSP data (solid lines) have been averaged into roughly a 100 km spatial resolution to be commensurate with the spatial scale of the AMIE fitting (dashed lines). The normalized root-mean-square (RMS) error and the correlation coefficient are also shown in each panel to serve as a quantitative measure of the AMIE fitting. The normalized RMS error is defined as $\sqrt{\langle Q_{\text{DMSP}} - Q_{\text{AMIE}} \rangle^2} / \sqrt{\langle Q_{\text{DMSP}}^2 \rangle}$, where Q represents a given parameter and $\langle \rangle$ symbolizes its mean value. In general, the along-track E-field component and the cross-track magnetic field perturbation yield the largest correlation coefficients and the smallest RMS errors, which is not surprising as they are part of the data inputs to AMIE. The two derived parameters, e.g., FAC and the Poynting flux, exhibit slightly smaller correlation coefficients and larger RMS errors, but the AMIE-derived values show a good agreement with the DMSP observations in terms of the overall morphology such as the large-scale downward and upward currents as well as the double humps of the Poynting flux along the spacecraft trajectories.

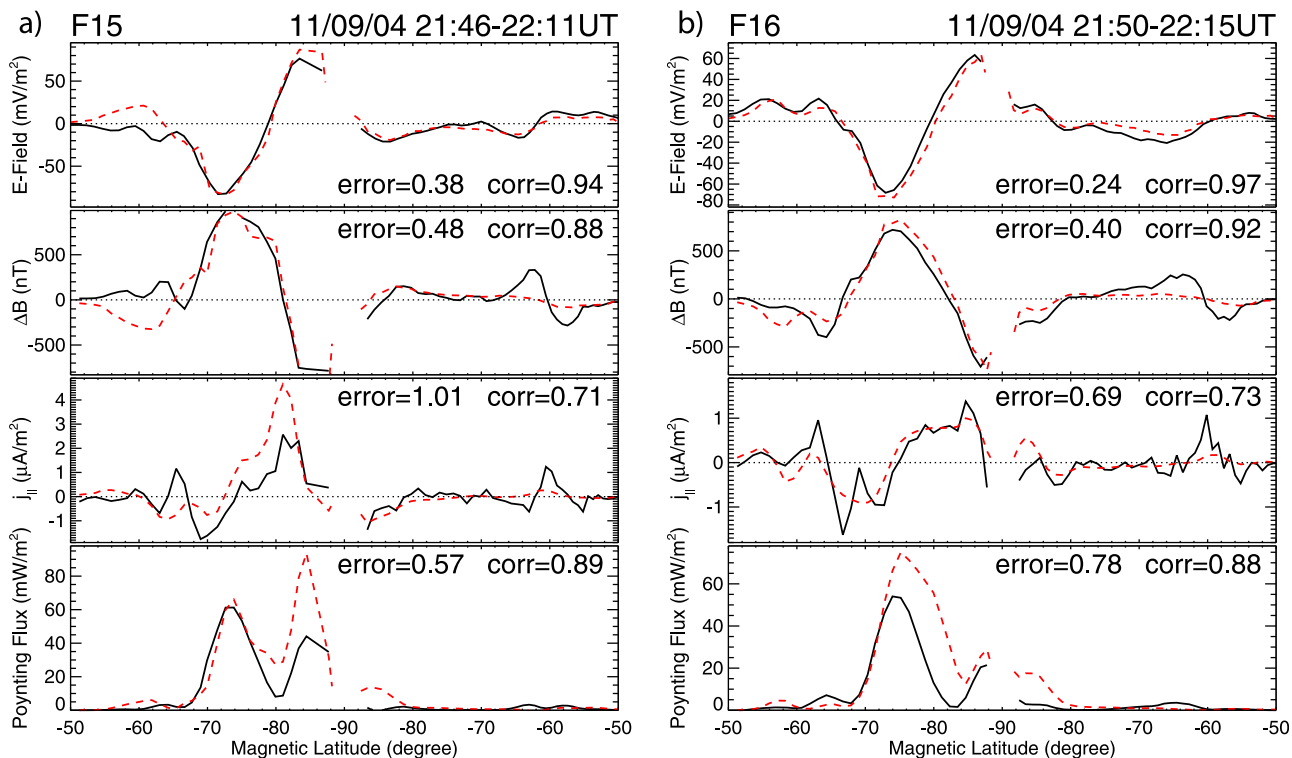


Figure 9. Comparison between the DMSP observed (solid lines) and AMIE fitted (dashed lines) parameters in the Southern Hemisphere around 22:05 UT: Plotted from top to bottom are the along-track E-field, the cross-track magnetic field perturbation, field-aligned currents, and the Poynting flux. Comparisons with (a) the F15 data and (b) the F16 data are shown. The values of the normalized RMS error (error) and the cross-correlation coefficient (corr) are shown in each panel.

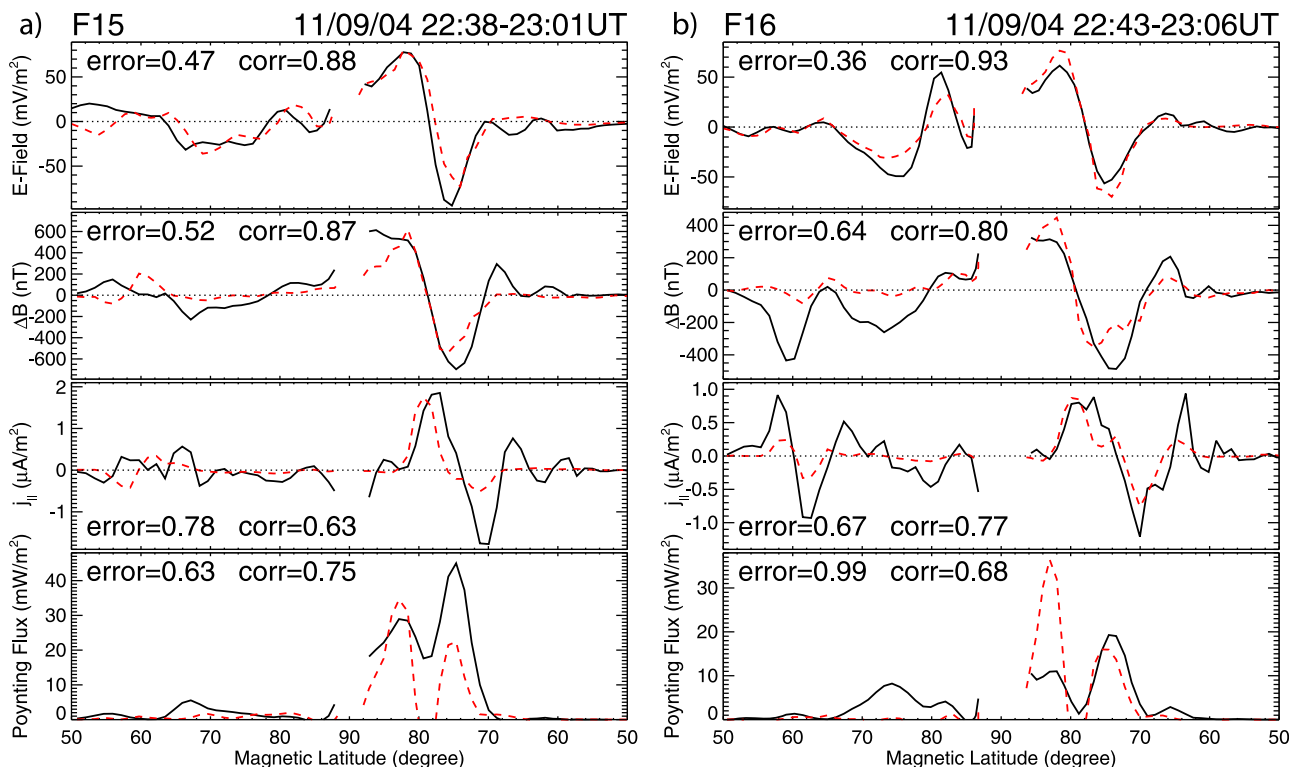


Figure 10. Same as Figure 9 but for the Northern Hemisphere at around 22:55 UT.

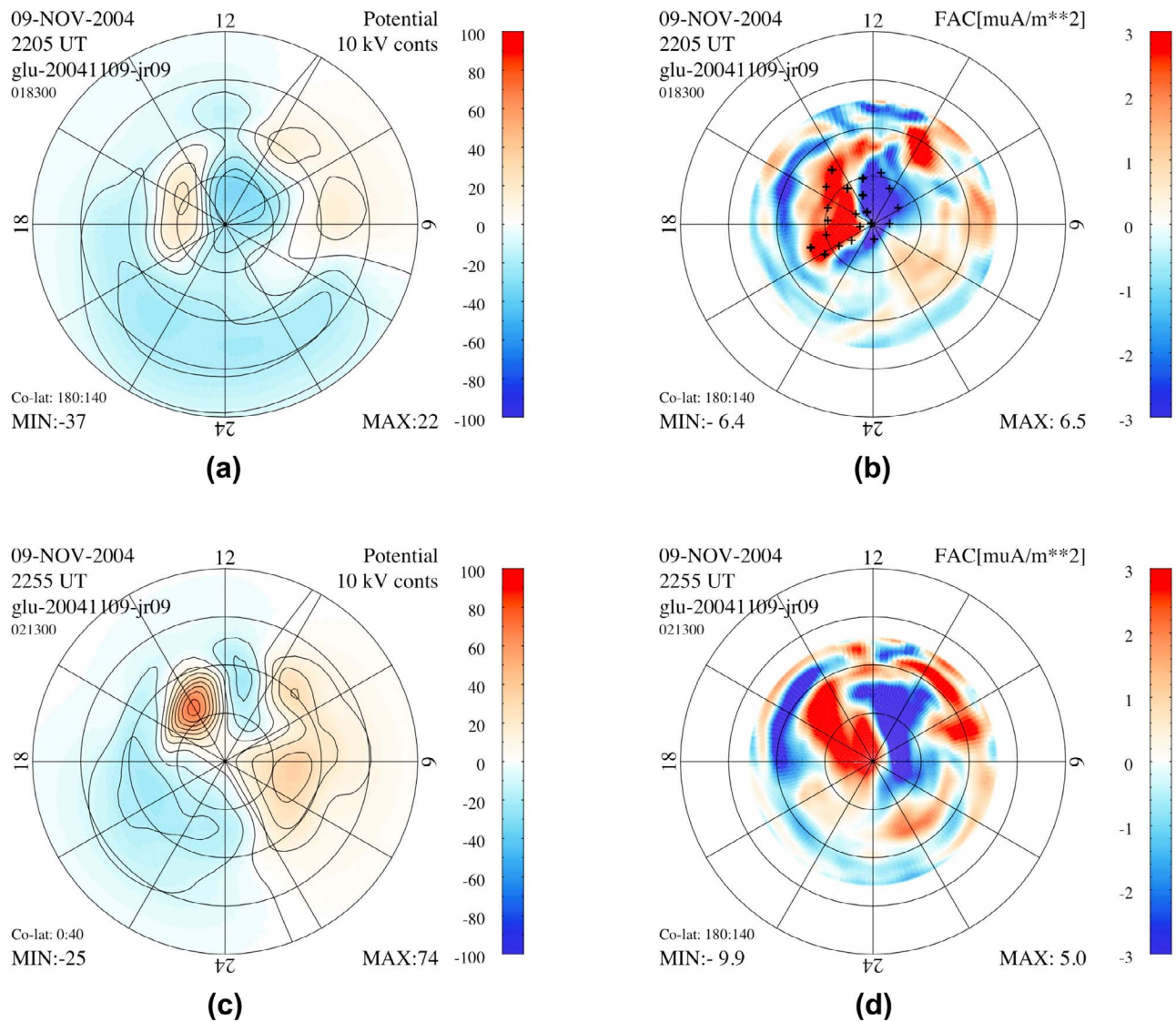


Figure 11. (a and b) Simulated patterns of plasma convection and FAC density at 22:05 UT in the Southern Hemisphere. (c and d) Simulated patterns of plasma convection and FAC density at 22:55 UT in the Northern Hemisphere. Positive values represent downward FACs, and negative values represent upward FACs. The “+” sign in Figure 11b marks roughly the edges of upward and downward NBZ currents.

2.4. Global MHD Simulations

[24] To help understand the coupling process in the solar wind-magnetosphere-ionosphere system during the event, global MHD simulations have been carried out using the OpenGGCM model [Raeder *et al.*, 1998, 2001, 2008; Raeder, 2003]. The model solves the resistive MHD equations on a nonuniform rectilinear grid, with a minimum grid spacing at GSE $y = 0$ and $z = 0$ in the Y and Z directions and at the subsolar magnetopause in the X direction. The smallest grid size is approximately $0.12 R_E$ in the X direction and $0.25 R_E$ in the Y and Z directions, respectively. For this study, the OpenGGCM is coupled to the Coupled Thermosphere Ionosphere Model (CTIP) [Fuller-Rowell *et al.*, 1996] to obtain self-consistent ionospheric conductances. Solar wind and IMF data from the ACE satellite are used to

drive the model. FACs are computed just outside a spherical surface of $3.7 R_E$ centered at the Earth and mapped to the low-altitude ionosphere using a dipole magnetic field. Ionospheric electric potential is then calculated based on the distribution of FACs along with ionospheric conductances from the CTIP module. The simulation starts at 17:00 UT on 9 November 2001 until the end of the day. To start up the simulation, constant solar wind and IMF values with a small southward IMF B_z are used in the first hour of the simulation. After that, the model applies the ACE data for the rest of the simulation, and the ACE data are propagated and prepared to conserve $\nabla \cdot \vec{B} = 0$ as described in the study by Raeder *et al.* [2001].

[25] Figure 11 displays the patterns of plasma convection and FACs from the MHD simulations, which can be

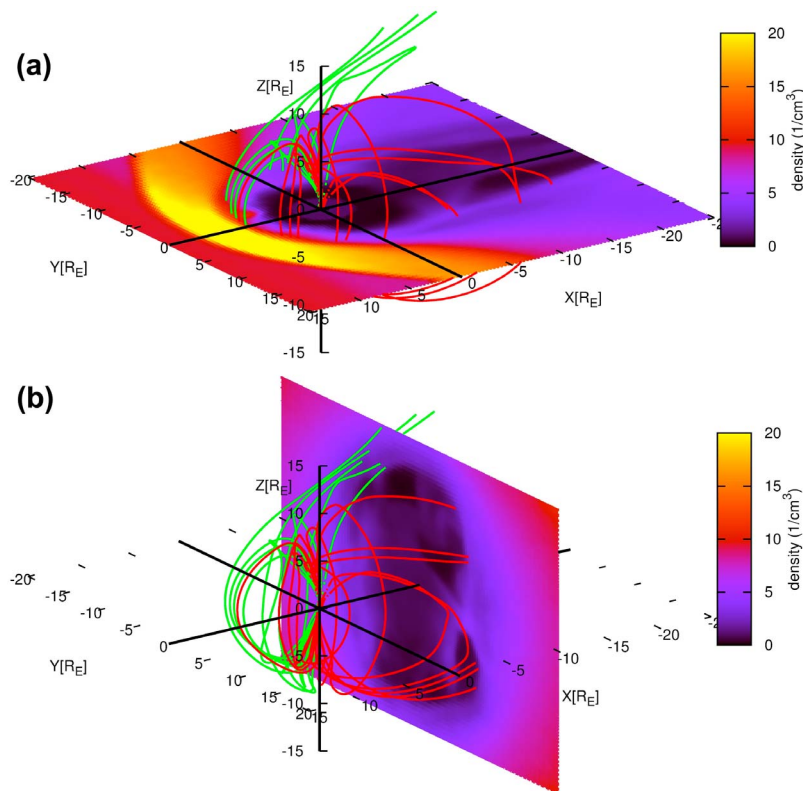


Figure 12. Magnetic field lines traced from the southern ionospheric footprints of the NBZ currents shown in Figure 11b. The red field lines are associated with the downward NBZ current, and the green field lines are for the upward NBZ current. The color image represents magnetospheric plasma density in per cubic centimeter (a) in the GSE equatorial plane and (b) in the GSE Y - Z plane at $x = -10 R_E$. The red ($\sim 10 \text{ cm}^{-3}$) region indicates the solar wind; the yellow ($> \sim 15 \text{ cm}^{-3}$) region indicates the magnetosheath; the blue-violet ($\sim 5 \text{ cm}^{-3}$) region indicates the boundary layer with a mix of magnetosheath and the magnetosphere plasma; and the dark ($< \sim 1 \text{ cm}^{-3}$) region corresponds to the inner magnetosphere, the CPS, and the tail lobe.

compared with the AMIE patterns shown in Figures 7 and 8. At 22:05 UT (Figures 11a and 11b), the simulations show that the southern polar region is dominated by two reverse-convection cells near the central polar region, which are very similar to those shown in Figure 7a but with a smaller cross-polar-cap potential drop of 59 kV compared to 97 kV in the AMIE pattern. In the subauroral zone, convection becomes much weaker as indicated by the coarser contour intervals, with the clockwise plasma circulation from dusk to early morning. The simulated FACs are shown in Figure 11b, depicting many small-scale features compared to the classic *Iijima-Potemra* pattern [*Iijima and Potemra, 1978*]. The dominant feature is a pair of FACs near the central polar region, which is again very similar to that shown in Figure 7b. Figures 11c and 11d are the patterns of plasma convection and FACs from the simulations at 22:55 UT in the Northern Hemisphere. Again, these patterns show a good qualitative agreement with the AMIE-derived patterns in Figures 8a and 8b with regard to the large-scale morphology, namely, both AMIE and the MHD simulations display the same reversed two-cell convection, along with a pair of NBZ currents occupying the central northern polar region. However, the simulated NBZ currents encompass a much bigger

portion of the polar region than the AMIE-derived NBZ currents do. The potential drop between the two reverse-convection cells is 99 kV, which is larger than the potential drop of 83 kV in the AMIE pattern.

[26] Encouraged by the agreement in general morphology between the simulations and the AMIE patterns, we further explore the simulation results to understand where in the magnetosphere the NBZ currents originate. For that purpose, we map the pair of NBZ currents to the magnetosphere along magnetic field lines. Figure 12 shows the field lines that are connected to the upward leg (in green) and downward leg (in red) of the NBZ currents, respectively. The footprints of these field lines are marked by the “+” signs shown in Figure 11b. The simulations reveal that the downward NBZ currents (red lines) map to the closed field line regions in the boundary layer and in the plasma sheet, whereas the upward NBZ currents (green lines) are partly from the closed boundary layer and are partly from the open tail lobe via the overdraped field lines.

[27] To further elucidate how exactly the interaction between the solar wind and magnetosphere leads to double-lobe reconnection in both the Northern and Southern Hemispheres, we again resort to the MHD simulations by

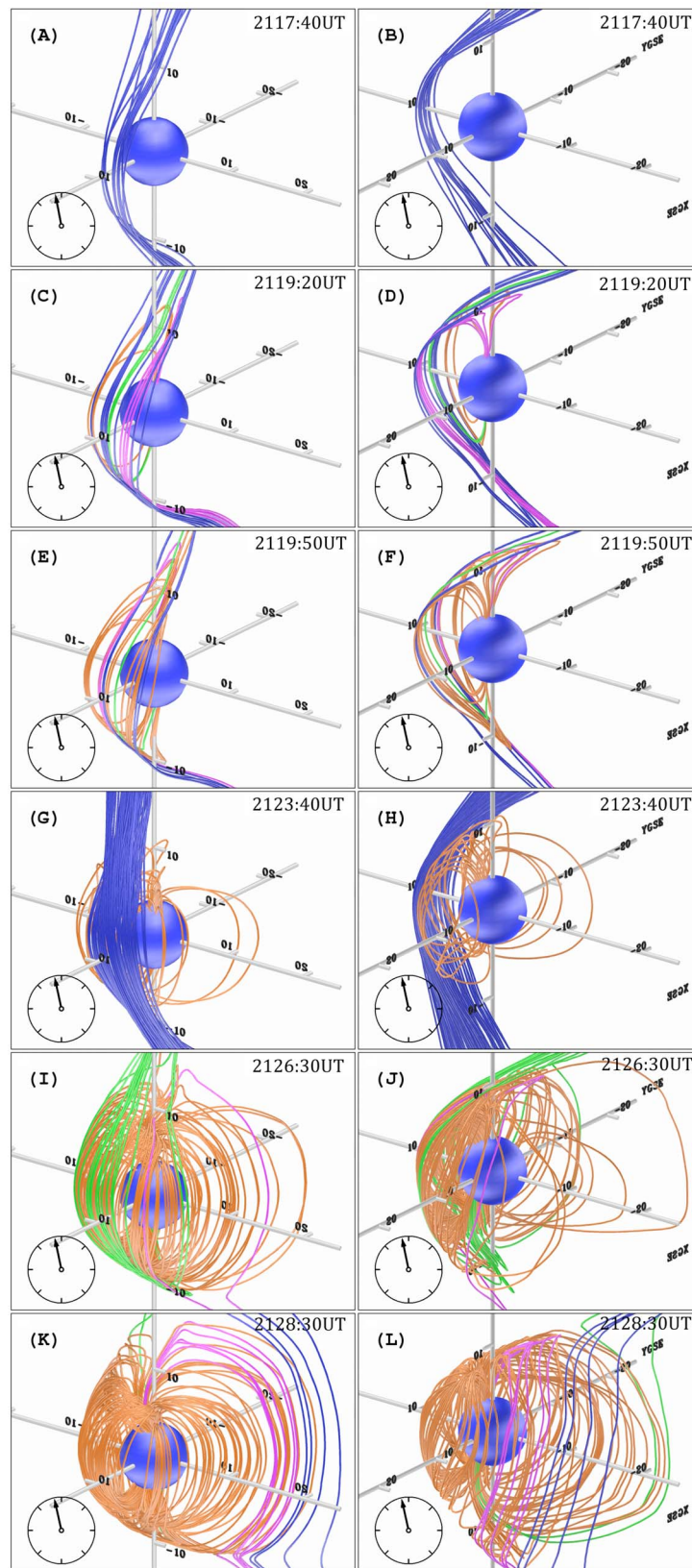


Figure 13. Renderings of magnetic field lines viewed from (left) 14:30 LT and from (right) 20:30 LT at selected UT times on 9 November 2004. The inserted dial plot indicates the corresponding IMF clock angle. The different color lines represent the different field line topology, with the dark blue lines for solar wind field lines, the magenta and green lines for open field lines, and the orange lines for closed field lines. The blue sphere at the center denotes the inner boundary of the MHD solution at $3.7 R_E$.

following field lines from the solar wind as they convect into the magnetosheath and reconnect with the magnetospheric field. More specifically, we launch a large number of fluid particles upstream of the magnetopause and follow them in time. Assuming that the frozen-in condition holds, a field line is connected to each of the fluid elements and convects along with it. This is, in general, a good assumption as long as the fluid element itself does not cross the reconnection diffusion region. For the fluid particles considered here, this is always the case because the fluid particles move close to the equatorial plane, whereas reconnection occurs at high latitudes. As a fluid particle is being traced in time, we monitor if the topology of the associated field line changes, in other words, if the field line reconnects. This is done by tracing the field line from the fluid element in both directions every few seconds and determining where its two ends are located. There are only four distinct topologies possible, namely, the field line is unconnected (solar wind type), it is connected to the northern or southern polar cap with the other end in the solar wind (open type), or it is connected to both polar caps (closed type). Any change in the type of the field line signifies that it has undergone reconnection because the fluid element has crossed a magnetic separator.

[28] Most of the solar wind field lines traced never reconnect with the magnetospheric field lines, and they simply drape over the magnetosphere and convect past it with the magnetosheath flow. However, a small subset of solar wind field lines will undergo reconnection. We disregard the field lines that never reconnect and only follow those that do. The total number of field lines traced is adjusted, so that only a few dozen are shown to make efficient visualization possible and to exhibit the essence of the process.

[29] Figure 13 shows renderings of those field lines at different times and from different perspectives. The left column corresponds to a view angle at 14:30 LT, whereas the right column corresponds to a viewing angle at 20:30 LT. The inserted dial plot shows the corresponding IMF clock angle. The color of the field lines indicates their topology. Solar wind-type field lines are in dark blue, closed field lines are in orange, and open field lines are in magenta for those rooted in the northern polar cap or in green for those rooted in the Southern Hemisphere. The blue sphere at the center denotes the inner boundary of the MHD solution at $3.7 R_E$.

[30] At 21:17:40 UT (Figures 13a and 13b), solar wind field lines are draping over the magnetosphere, but they have not yet reconnected with geomagnetic field lines. One hundred seconds later, at 21:19:20 UT (Figures 13c and 13d), most of the solar wind field lines have undergone reconnection. There are open south (magenta) and open north (green) field lines resulting from reconnection in either the northern or southern polar cap, as well as closed field lines. There is no preferred order in which the field lines reconnect, as proposed in section 1. It appears to be rather random whether reconnection first occurs in the Northern or Southern Hemisphere. At 21:19:50 UT (Figures 13e and 13f), virtually all the solar field lines have reconnected, and most of them have reconnected in both the hemispheres to form closed field lines. Note that so far we have only traced one bundle of field lines here, and no new field lines were introduced between Figures 13a and 13b and Figures 13e and 13f.

[31] In Figures 13g and 13h (21:23:40 UT), we introduce a new set of solar wind field lines, but we keep tracing the previous bundle of field lines as well. By now, these old field lines have all undergone double-lobe reconnection and have become closed. The new field lines are draped over the magnetosphere but have not yet reconnected. At the next snapshot at 21:26:30 UT (Figures 13i and 13j), the reconnection process is in progress. Some of the new field lines have already reconnected twice and have become closed, but some become open field lines as they have reconnected just once. It is interesting to point out that while some of those open field lines have formed by reconnection between geomagnetic field lines and solar wind field lines, others have formed by reconnection between solar wind field lines and field lines that had been previously closed. Although these previously closed field lines are technically also geomagnetic field lines, they are all situated very close to the magnetopause because they have not yet had time to convect deeper into the magnetosphere. In Figures 13k and 13l (21:28:30 UT), this becomes even clearer. There are several field lines that look like the closed (orange) field lines, but they have already been detached by reconnection near one of the cusps. When these field lines reconnect at the other cusp too, they will be completely detached and become of solar wind-type again. There are several of such field lines in Figures 13k and 13l, distinguished by their dark blue color. One can also find more detailed information about the behaviors of magnetic field lines involved in cusp reconnection in the MHD study by *Li et al.* [2008 and references therein].

3. Summary and Discussion

[32] Although sunward or reverse convection has been observed and studied by numerous researchers, this article is among the first to report the formation of reversed two-cell convection in the Northern and Southern Hemispheres simultaneously that lasted for nearly 2 hours after the IMF turned strongly northward. As postulated by the overdraped lobe model, the combination of seasonal effect (which favors the Southern Hemisphere) and the IMF B_x effect (which favors the Northern Hemisphere) may have constituted a necessary circumstance under which reverse convection can take place in both the hemispheres.

[33] The plasma characteristics observed by the DMSP spacecraft indicate that the reverse plasma flows originate in the region where precipitating electrons resemble those of the BPS but with smaller number flux, and the precipitating ions are too weak to be detectable by the DMSP spacecraft. To distinguish it from the normal BPS, we have named the region as the NBZBL. The MHD simulations shown in Figure 13 imply that the region consists of both open and closed field lines. When an originally closed plasma sheet field line reconnects with the IMF to form an overdraped field line, part of the plasma sheet electrons along the flux tube are lost in the process, causing reduced electron number flux along the newly opened field line. If the overdraped field line reconnects soon enough in the opposite hemisphere and becomes closed again, the remnant plasma sheet electrons within the flux tube are retained. The plasma sheet ions, on the other hand, are mostly lost partly to the reconnection

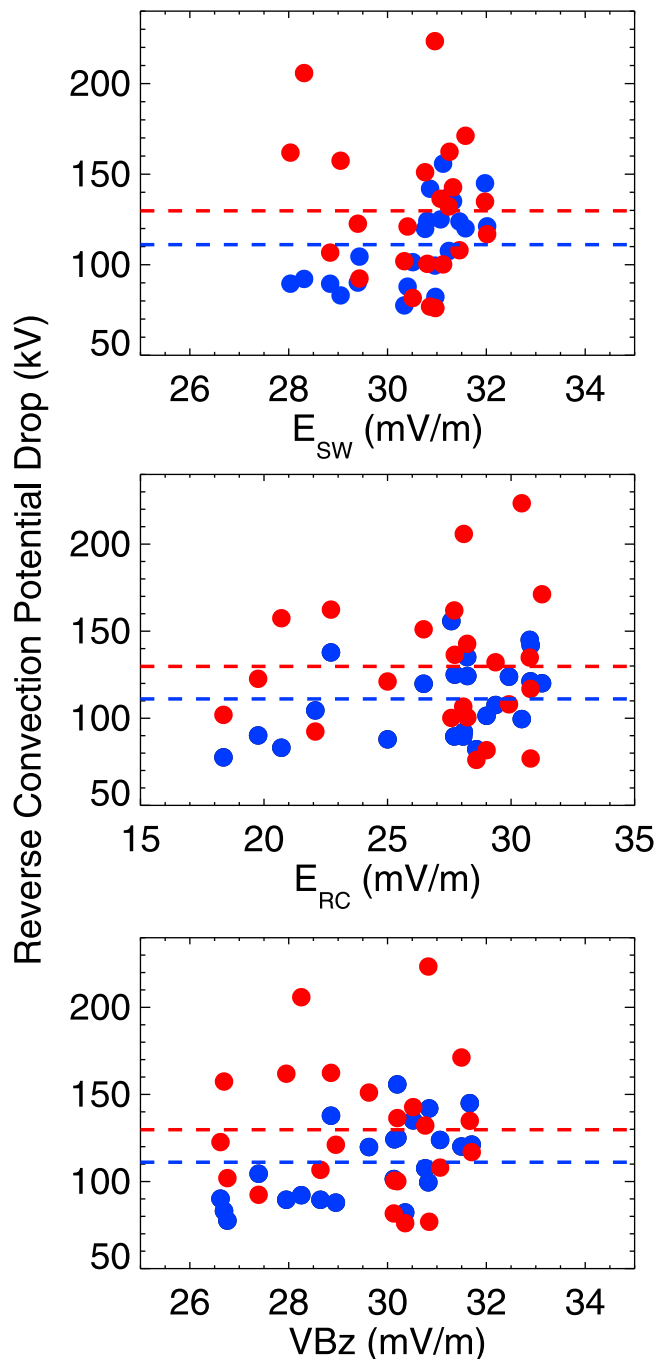


Figure 14. Scatterplots of reverse potential drops found for 9 November 2004 versus the three different coupling functions (i.e., E_{SW} , E_{RC} , and VBz). The red dots represent reverse potential drops in the Southern Hemisphere, and the blue dots for reverse potential drops in the Northern Hemisphere. The red and blue dashed lines are the average reverse potential drops in the two hemispheres.

process and partly to the cross-field scatter because of their much larger gyroradius compared to electrons. For those overdraped field lines that never reconnect in the opposite hemisphere, the plasma sheet electrons are eventually all lost to the solar wind along the open field lines

as they are dragged tailward by the solar wind. Therefore, it is our interpretation that the NBZBL is a consequence of the double-lobe reconnection.

[34] The mix of open and closed field lines in the NBZBL as shown in the simulations makes the identification of plasma source regions difficult. Whether the NBZBL is open or closed depends on the IMF orientation as well as the seasonal effect associated with the dipole tilt that permit double-lobe reconnection to occur in both the hemispheres. This also explains why previous studies have found the origin of precipitating particles associated with reverse convection to be of plasma sheet proper at some times but magnetosheath-like at other times [Newell *et al.*, 1997; Eriksson *et al.*, 2006]. A recent article by Zhang *et al.* [2009] shows a case study in which the polar ionosphere evolved from an open polar cap, with almost no precipitation of any energetic particles, to a region filled with discrete auroral arcs several hours after the IMF turned from southward to strongly northward, which the authors interpreted as evidence of the disappearance of the polar cap resulting from a fully closed magnetosphere.

[35] Double-lobe reconnection often takes place when the IMF clock angle is less than 10° [e.g., Imber *et al.*, 2006; Provan *et al.*, 2005]. The overdraped lobe model also expects double-lobe reconnection most likely to occur when the IMF B_y component is very small. Our study, however, shows that the reversed two-cell convection patterns were formed when the IMF clock was less than 28° . Furthermore, sunward flows were observed by the DMSP spacecraft in both the hemispheres even when the IMF clock angle was as large as 50° . The fact that the reversed two-cell convection was observed for such large clock angles may be attributed to the unusually large B_z value, which was around 35–40 nT. In addition, the solar wind dynamic pressure was more than 10 nPa, roughly five times its nominal value. Enhanced solar wind dynamic pressure is known to increase the reconnection rate [e.g., Siscoe *et al.*, 2002].

[36] There have been ample observations showing saturation of the cross-polar-cap potential drop under strongly southward IMF [Russell *et al.*, 2001; Shepherd *et al.*, 2003; Hairston *et al.*, 2003, 2005]. Recent studies revealed that the potential drop across the two reverse-convection cells saturates as well under strongly northward IMF conditions. On the basis of the observations from the SuperDARN, Wilder *et al.* [2009] derived a coupling function for the electric field associated with reverse convection under northward IMF, $E_{RC} = VB_T \cos^4 \theta$, where V is the solar wind speed, $B_T = \sqrt{B_y^2 + B_z^2}$, and θ is the IMF clock angle.

By analyzing the DMSP polar passes from the period 1996 to 2002, Sundberg *et al.* [2009] obtained a similar coupling function but without the IMF clock angle dependency: $E_{SW} = VB_T$. Both studies found that the reverse-convection potential saturates with increasing northward IMF, and the saturation potential is approximately 20 kV based on SuperDARN and about 60 kV based on DMSP. A statistical study of the DE 2 satellite data by Taguchi and Hoffman [1995] also depicted a clear trend of saturation in reverse-convection potential, with a saturation potential value around 70 kV. To place our case in the context of the previous studies, Figure 14 shows the scatterplots of the

reverse-convection potential drops found on 9 November 2004 versus three types of coupling functions, that is, E_{SW} , E_{RC} , and VB_z . Note that the range of the various coupling functions plotted here is far beyond their respective threshold values for nonlinear effects found by previous studies, namely, $E_{SW} > 6$ mV/m and $E_{RC} > 20$ kV/ R_E (or ~ 3 mV/m). A couple of important features can be drawn from the scatterplots: (1) There is no clear dependence of the reverse potential drop on any of the coupling functions, an indication that the reverse potential drop is well into the presumed saturation zone; (2) the reverse potential drop exceeds 100 kV in both the hemispheres, substantially larger than any previous reported values; and (3) on average, the reverse potential is larger in the Southern (Summer) Hemisphere than in the Northern (Winter) Hemisphere, consistent with the previous findings that reverse convection occurs preferentially in the Summer Hemisphere.

[37] **Acknowledgments.** We wish to acknowledge the International Real-time Magnetic Observatory Network for the INTERMAGNET magnetometer network, the Geophysical Institute of the University of Alaska for the Alaska magnetometer stations, the Solar-Terrestrial Environment Laboratory of the Nagoya University for the 210 magnetic meridian chain, the Finnish Meteorological Institute for the IMAGE chain, the Canadian Space Agency for CARISMA magnetometer network, and the Space Plasma Environment and Radio Science (SPEARS) in the Department of Communication Systems at the Lancaster University for the SAMNET magnetometer chain, and the Danish Meteorological Institute for the Greenland magnetometer stations. J. Posch at Augsburg College and O. Troshichev at the Arctic and Antarctic Research Institute in Russia provided additional ground magnetometer data used in this study. We also acknowledge the CEDAR data based at the National Center for Atmospheric Research (NCAR) for providing the $F_{10.7}$ and auroral hemispheric power indices used in this study. The ACE solar wind and IMF key parameters were obtained from the NASA CDAW website. The DMSP particle detectors were designed by Dave Hardy of Air Force Research Laboratory, and data were obtained from JHU/APL. The research at UNH was supported by grants OCI-0749125 and ATM-0639658 from the National Science Foundation (NSF) and by grant NNX10AL07G from the National Aeronautics and Space Administration (NASA). Work at UTA was supported by NSF grant ATM0955629. Work at HAO/NCAR was supported in part by NASA's Heliophysics Guest Investigators Program under grant NNNH09AK621. NCAR is sponsored by the NSF.

[38] Robert Lysak thanks Gabrielle Provan and another reviewer for their assistance in evaluating this paper.

References

- Burch, J. L., P. H. Reiff, R. W. Spiro, R. A. Heelis, and S. A. Fields (1980), Cusp region particle precipitation and ion convection for northward interplanetary magnetic field, *Geophys. Res. Lett.*, *7*, 393–396, doi:10.1029/GL007i005p00393.
- Burton, R. K., R. L. McPherron, and C. T. Russell (1975), An empirical relationship between interplanetary conditions and *Dst*, *J. Geophys. Res.*, *80*, 4204–4214, doi:10.1029/JA080i031p04204.
- Bythrow, P. F., W. J. Burke, T. A. Potemra, L. J. Zanetti, and A. T. Y. Lui (1985), Ionospheric evidence for irregular reconnection and turbulent plasma flows in the magnetotail during periods of northward interplanetary magnetic field, *J. Geophys. Res.*, *90*, 5319–5325, doi:10.1029/JA090iA06p05319.
- Christensen, A. B., et al. (2003), Initial observations with the Global Ultraviolet Imager (GUVI) in the NASA TIMED satellite mission, *J. Geophys. Res.*, *108*(A12), 1451, doi:10.1029/2003JA009918.
- Cowley, S. W. H. (1981), Magnetospheric and ionospheric flow and the interplanetary magnetic field, the physics basis of the ionosphere in the solar-terrestrial system, *AGARD Conf. Proc.*, *295*, 4, 1–14.
- Cowley, S. W. H. (1983), Interpretation of observed relations between solar wind characteristics and effects at ionospheric altitudes, in *High Latitude Space Plasma Physics*, edited by B. Hultqvist and T. Hagfors, pp. 225–249, Plenum, New York.
- Crooker, N. U. (1992), Reverse convection, *J. Geophys. Res.*, *97*, 19,363–19,372, doi:10.1029/92JA01532.
- Crooker, N. U., and F. J. Rich (1993), Lobe cell convection as a summer phenomenon, *J. Geophys. Res.*, *98*, 13,403–13,407, doi:10.1029/93JA01037.
- Cummock, J. A., R. A. Heelis, M. R. Hairston, and P. T. Newell (1995), High-latitude ionospheric convection pattern during steady northward interplanetary magnetic field, *J. Geophys. Res.*, *100*, 14,537–14,555, doi:10.1029/94JA03318.
- Deng, Y., G. Lu, Y.-S. Kwak, E. Sutton, J. Forbes, and S. Solomon (2009), Reversed ionospheric convections during the November 2004 storm: Impact on the upper atmosphere, *J. Geophys. Res.*, *114*, A07313, doi:10.1029/2008JA013793.
- Dungey, J. W. (1963), The structure of the exosphere or adventures in velocity space, in *Geophysics: The Earth's Environment*, edited by C. De Witt et al., pp. 526–535, Gordon and Breach, Newark, N. J.
- Eriksson, S., G. Provan, F. J. Rich, M. Lester, S. E. Milan, S. Massetti, J. T. Gosling, M. W. Dunlop, and H. Rème (2006), Electrodynamics of a split-transpolar aurora, *J. Geophys. Res.*, *111*, A11319, doi:10.1029/2006JA011976.
- Foster, J. C., J. M. Holt, R. G. Musgrave, and D. S. Evans (1986), Ionospheric convection associated with discrete levels of particle precipitation, *Geophys. Res. Lett.*, *13*, 656–659, doi:10.1029/GL013i007p00656.
- Fuller-Rowell, T. J., and D. S. Evans (1987), Height-integrated Pedersen and Hall conductivity patterns inferred from the TIROS-NOAA satellite data, *J. Geophys. Res.*, *92*, 7606–7618, doi:10.1029/JA092iA07p07606.
- Fuller-Rowell, T. J., M. V. Codrescu, H. Rishbeth, R. J. Moffett, and S. Quegan (1996), On the seasonal response of the thermosphere and ionosphere to geomagnetic storms, *J. Geophys. Res.*, *101*, 2343–2353, doi:10.1029/95JA01614.
- Hairston, M. R., and R. A. Heelis (1993), High-latitude electric field studies using DMSP data, *Rep. PL-TR-93-2036*, 45 pp., Phillips Lab., Hanscom AFB, Mass.
- Hairston, M. R., T. W. Hill, and R. A. Heelis (2003), Observed saturation of the ionospheric polar cap potential during the 31 March 2001 storm, *Geophys. Res. Lett.*, *30*(6), 1325, doi:10.1029/2002GL015894.
- Hairston, M. R., K. A. Drake, and R. Skoug (2005), Saturation of the ionospheric polar cap potential during the October–November 2003 superstorms, *J. Geophys. Res.*, *110*, A09S26, doi:10.1029/2004JA010864.
- Hardy, D. A., L. K. Schmitt, M. S. Gussenhoven, F. J. Marshall, H. C. Yeh, T. L. Schumaker, A. Hube, and J. Pantazis (1984), Precipitating electron and ion detectors (SSJ/4) for the block 5D/flights 6–10 DMSP satellites: Calibration and data presentation, *Rep. AFGL-TR-84-0317*, Air Force Geophys. Lab., Bedford, Mass.
- Heelis, R. A., and M. R. Hairston (1990), Studies of ionospheric dynamics utilizing data from DMSP, *Rep. GL-TR-90-0047*, 39 pp., Geophys. Lab., Hanscom AFB, Mass.
- Hu, H., T. K. Yeoman, M. Lester, R. Liu, H. Yang, and A. Grocott (2006), Dayside flow bursts and high-latitude reconnection when the IMF is strongly northward, *Ann. Geophys.*, *24*, 2227–2242, doi:10.5194/angeo-24-2227-2006.
- Iijima, T., and T. A. Potemra (1978), Large-scale characteristics of field-aligned currents associated with substorms, *J. Geophys. Res.*, *83*, 599–615, doi:10.1029/JA083iA02p00599.
- Iijima, T., T. A. Potemra, L. J. Zanetti, and P. F. Bythrow (1984), Large-scale Birkeland currents in the dayside polar region during strongly northward IMF: A new Birkeland current system, *J. Geophys. Res.*, *89*, 7441–7452, doi:10.1029/JA089iA09p07441.
- Imber, S. M., S. E. Milan, and B. Hubert (2006), The auroral and ionospheric flow signatures of dual lobe reconnection, *Ann. Geophys.*, *24*, 3115–3129, doi:10.5194/angeo-24-3115-2006.
- Knipp, D. J., et al. (1993), Ionospheric convection response to slow, strong variations in a northward interplanetary magnetic field: A case study for January 14, 1988, *J. Geophys. Res.*, *98*, 19,273–19,292, doi:10.1029/93JA01010.
- Li, W., J. Raeder, M. F. Thomsen, and B. Lavraud (2008), Solar wind plasma entry into the magnetosphere under northward IMF conditions, *J. Geophys. Res.*, *113*, A04204, doi:10.1029/2007JA012604.
- Lu, G., et al. (1994), Interhemispheric asymmetry of the high-latitude ionospheric convection pattern, *J. Geophys. Res.*, *99*, 6491–6510, doi:10.1029/93JA03441.
- Lu, G., A. D. Richmond, B. A. Emery, and R. G. Roble (1995), Magnetosphere-ionosphere-thermosphere coupling: Effect of neutral winds on energy transfer and field-aligned current, *J. Geophys. Res.*, *100*, 19,643–19,659, doi:10.1029/95JA00766.
- Lu, G., et al. (1996), High-latitude ionospheric electrodynamic as determined by the assimilative mapping of ionospheric electrodynamic procedure for the conjunctive SUNDIAL/ATLAS 1/GEM period of March 28–29, 1992, *J. Geophys. Res.*, *101*, 26,697–26,718, doi:10.1029/96JA00513.
- Lu, G., A. D. Richmond, J. M. Ruohoniemi, R. A. Greenwald, M. Hairston, F. J. Rich, and D. S. Evans (2001), An investigation of the influence of data and model inputs on assimilative mapping of ionospheric electrodynamic, *J. Geophys. Res.*, *106*, 417–433, doi:10.1029/2000JA000606.

- Milan, S. E., M. Lester, S. W. H. Cowley, and M. Brittnacher (2000), Day-side convection and auroral morphology during an interval of northward interplanetary magnetic field, *Ann. Geophys.*, *18*, 436–444, doi:10.1007/s00585-000-0436-9.
- Newell, P. T., and C.-I. Meng (1992), Mapping the dayside ionosphere to the magnetosphere according to particle precipitation characteristics, *Geophys. Res. Lett.*, *19*, 609–612, doi:10.1029/92GL00404.
- Newell, P. T., W. J. Burke, C.-I. Meng, E. R. Sanchez, and M. E. Greenspan (1991), Identification and observations of the plasma mantle at low altitude, *J. Geophys. Res.*, *96*, 35–45, doi:10.1029/90JA01760.
- Newell, P. T., D. Xu, C.-I. Meng, and M. G. Kivelson (1997), Dynamical polar cap: A unifying approach, *J. Geophys. Res.*, *102*, 127–139, doi:10.1029/96JA03045.
- Paxton, L. J., D. Morrison, Y. Zhang, H. Kil, B. Wolven, B. S. Ogorzalek, D. C. Humm, and C.-I. Meng (2002), Validation of remote sensing products produced by the Special Sensor Ultraviolet Scanning Imager (SSUSI): A far UV-imaging spectrograph on DMSP F-16, in *Optical Spectroscopic Techniques, Remote Sensing, and Instrumentation for Atmospheric and Space Research IV*, edited by A. M. Larar and M. G. Mlynczak, *Proc. SPIE Int. Soc. Opt. Eng.*, *4485*, 338–348.
- Provan, G., M. Lester, A. Grocott, and S. W. H. Cowley (2005), Pulsed flows observed during an interval of prolonged northward IMF, *Ann. Geophys.*, *23*, 1207–1255, Sref-ID: 1432-0576/ag/2005-23-1207.
- Raeder, J. (2003), Global magnetohydrodynamics—A tutorial, in *Space Plasma Simulation*, edited by J. Büchner et al., pp. 212–246, Springer, Berlin, doi:10.1007/3-540-36530-3_11.
- Raeder, J., J. Berchem, and M. Ashour-Abdalla (1998), The geospace environment modeling grand challenge: Results from global geospace circulation model, *J. Geophys. Res.*, *103*, 14,787–14,797, doi:10.1029/98JA00014.
- Raeder, J., R. L. McPherron, L. A. Frank, S. Kokubun, G. Lu, T. Mukai, W. R. Paterson, J. B. Sigwarth, H. J. Singer, and J. A. Slavin (2001), Global simulation of the geospace environment modeling substorm challenge event, *J. Geophys. Res.*, *106*, 381–395, doi:10.1029/2000JA000605.
- Raeder, J., D. Larson, W. H. Li, E. L. Kepko, and T. Fuller-Rowell (2008), OpenGGCM simulations for the THEMIS mission, *Space Sci. Rev.*, *141*, 535–555, doi:10.1007/s11214-008-9421-5.
- Reiff, P. H. (1982), Sunward convection in both polar caps, *J. Geophys. Res.*, *87*, 5976–5980, doi:10.1029/JA087iA08p05976.
- Reiff, P. H., T. W. Hill, and J. L. Burch (1977), Solar wind plasma injection at the dayside magnetospheric cusp, *J. Geophys. Res.*, *82*, 479–491, doi:10.1029/JA082i004p00479.
- Reiff, P. H., J. L. Burch, and R. W. Spiro (1980), Cusp proton signatures and the interplanetary magnetic field, *J. Geophys. Res.*, *85*, 5997–6005, doi:10.1029/JA085iA11p05997.
- Richardson, I. G., and H. V. Cane (2010), Near-earth interplanetary coronal mass ejections during solar cycle 23 (1996–2009), catalog and summary of properties, *Sol. Phys.*, *264*, 189–237, doi:10.1007/s11207-010-9568-6.
- Richmond, A. D. (2010), On the ionospheric application of Poynting's theorem, *J. Geophys. Res.*, *115*, A10311, doi:10.1029/2010JA015768.
- Richmond, A. D., and Y. Kamide (1988), Mapping electrodynamic features of the high-latitude ionosphere from localized observations: Technique, *J. Geophys. Res.*, *93*, 5741–5759, doi:10.1029/JA093iA06p05741.
- Russell, C. T., J. G. Luhmann, and G. Lu (2001), Nonlinear response of the polar ionosphere to large values of the interplanetary electric field, *J. Geophys. Res.*, *106*, 18,495–18,504, doi:10.1029/2001JA900053.
- Shepherd, S. G., J. M. Ruohoniemi, and R. A. Greenwald (2003), Testing the Hill model of transpolar potential with Super Dual Auroral Radar Network observations, *Geophys. Res. Lett.*, *30*(1), 1002, doi:10.1029/2002GL015426.
- Siscoe, G. L., N. U. Crooker, and K. D. Siebert (2002), Transpolar potential saturation: Roles of region 1 current system and solar wind ram pressure, *J. Geophys. Res.*, *107*(A10), 1321, doi:10.1029/2001JA009176.
- Sundberg, K. Å. T., J. A. Cumnock, and L. G. Blomberg (2009), Reverse convection potential: A statistical study of the general properties of lobe reconnection and saturation effects during northward IMF, *J. Geophys. Res.*, *114*, A06205, doi:10.1029/2008JA013838.
- Taguchi, S., and R. A. Hoffman (1995), B_x control of polar cap potential for northward interplanetary magnetic field, *J. Geophys. Res.*, *100*, 19,313–19,320, doi:10.1029/95JA01085.
- Thayer, J. P., J. F. Vickrey, R. A. Heelis, and J. B. Gary (1995), Interpretation and modeling of the high-latitude electromagnetic energy flux, *J. Geophys. Res.*, *100*, 19,715–19,728, doi:10.1029/95JA01159.
- Wilder, F. D., C. R. Clauer, and J. B. H. Baker (2009), Reverse convection potential saturation during northward IMF under various driving conditions, *J. Geophys. Res.*, *114*, A08209, doi:10.1029/2009JA014266.
- Zhang, Y., and L. J. Paxton (2008), An empirical Kp -dependent global auroral model based on TIMED/GUVI FUV data, *J. Atmos. Sol. Terr. Phys.*, *70*, 1231–1242, doi:10.1016/j.jastp.2008.03.008.
- Zhang, Y., L. J. Paxton, P. T. Newell, and C.-I. Meng (2009), Does the polar cap disappear under an extended strong northward IMF?, *J. Atmos. Sol. Terr. Phys.*, *71*, 2006–2012, doi:10.1016/j.jastp.2009.09.005.
- Y. Deng, Department of Physics, University of Texas at Arlington, 502 Yates St., Arlington, TX 76019, USA.
- M. Hairston, Center for Space Sciences, University of Texas at Dallas, 800 W. Campbell Rd., WT15, Richardson, TX 75080-3021, USA.
- W. H. Li and J. Raeder, Space Science Center, Department of Physics, University of New Hampshire, 8 College Rd., Durham, NH 03824, USA.
- G. Lu, High Altitude Observatory, National Center for Atmospheric Research, 3080 Center Green, Boulder, CO 80301, USA. (ganglu@ucar.edu)
- P. Newell, L. Paxton, and Y. L. Zhang, Johns Hopkins University Applied Physics Laboratory, 11100 Johns Hopkins Rd., Laurel, MD 20723, USA.
- D. Ober, Air Force Research Laboratory, 3550 Aberdeen Ave. SE, Kirtland Air Force Base, NM 87117, USA.
- F. Rich, Massachusetts Institute of Technology Lincoln Laboratory, 244 Wood St., Lexington, MA 02421, USA.
- J. M. Ruohoniemi, Department of Engineering, Virginia Polytechnic Institute and State University, 302 Whittemore Hall, Blacksburg, VA 24061, USA.